Chem Soc Rev

Dehydration, Dehydrogenation, and Condensation of Alcohols on Supported Oxide Catalysts Based on Cyclic (WO3)3 and (MoO3)3 Clusters

Journal:	*Chemical Society Reviews*
Manuscript ID:	CS-REV-12-2013-060445.R2
Article Type:	Review Article
Date Submitted by the Author:	09-Feb-2014
Complete List of Authors:	Rousseau, Roger; Pacific Northwest National Laboratory, Dixon, David; University of Alabama, Chemistry Kay, Bruce; Pacific Northwest National Laboratory, Fundamental and Computational Sciences Directorate Dohnalek, Zdenek; Pacific Northwest National Laboratory, Fundamental and Computational Sciences Directorate

Journal Name

RSCPublishing

ARTICLE

Dehydration, Dehydrogenation, and Condensation of Alcohols on Supported Oxide Catalysts Based on Cyclic $(WO_3)_3$ and $(MoO_3)_3$ Clusters

Roger Rousseau,[a] David A Dixon,[b] Bruce D. Kay,[a] and Zdenek Dohnálek[a]

Cite this: DOI: 10.1039/x0xx00000x

Received 00th January 2012,
Accepted 00th January 2012

DOI: 10.1039/x0xx00000x

www.rsc.org/

Supported early transition metal oxides have important applications in numerous catalytic reactions. In this article we review the synthesis and activity of well-defined model WO_3 and MoO_3 catalysts that are prepared *via* deposition of cyclic gas-phase $(WO_3)_3$ and $(MoO_3)_3$ clusters generated by sublimation of WO_3 and MoO_3 powders. Conversion of small aliphatic alcohols to alkenes, aldehydes/ketones, and ethers is employed to probe the structure-activity relationships on model catalysts ranging from unsupported $(WO_3)_3$ and $(MoO_3)_3$ clusters embedded in alcohol matrices, to $(WO_3)_3$ clusters supported on surfaces of other oxides, and epitaxial and nanoporous WO_3 films. Detailed theoretical calculations reveal the underlying reaction mechanisms and provide insight into the origin of the differences in the WO_3 and MoO_3 reactivity. The catalytic activity for a range of interrogated $(WO_3)_3$ motifs (from unsupported clusters to nanoporous films) further sheds light onto the role structure and binding of $(WO_3)_3$ clusters with the support play in determining their catalytic activity.

1. Introduction

Mixed metal oxides containing WO_3 and MoO_3 are ubiquitous in catalytic chemical conversions.[1-12] For instance, WO_x supported on oxides such as ZrO_2,[13-17] Al_2O_3,[17, 18] SiO_2,[19] TiO_2,[16] and SnO_2 [20] have shown pronounced catalytic activity in isomerization of alkanes and alkenes, dehydration of alcohols, hydration of alkenes, partial oxidation of alcohols, selective reduction of nitric oxide, and metathesis of alkenes. In a similar vein, supported MoO_3 catalysts have been employed for a multitude of different reactions such as methanol oxidation to formaldehyde,[21] selective oxidation/ammoxidation of propylene,[22, 23] alkene isomerization,[24] and hydrogenation.[25] In addition to these thermal catalytic processes, both WO_3 and MoO_3 when supported on photoactive supports such as TiO_2 have even been shown to be active as photocatalysts.[26] Despite the intense interest in these materials, obtaining an atomic level understanding of the complex chemistry of these catalysts has been a grand scientific challenge due to the innate difficulty of obtaining well characterized model systems on which to perform detailed chemical and kinetic analysis to relate structure and catalytic activity.[11, 17, 27-33]

Despite the complexity of high surface area catalysts characterization, a certain level of understanding has been reached on how their catalytic activity relates to factors such as the size of oxide domains,[13, 34, 35] the presence of hydroxyl groups,[20, 36, 37] and the role of redox active W and Mo centers.[38, 39] In general, the catalytic activity of oxide-supported highly dispersed MO_x (M = W and Mo) catalysts has been associated with the presence of protons (Brønsted acid sites),[20, 34, 37] where the catalytic activity is strongly influenced by the type of oxide support. Brønsted acidity has recently been reported to be an important component in catalytic dehydration of alcohols by tungsten polyoxometalate clusters,[40, 41] where a key intermediate is found to be a W-bound alkoxy group similar to that proposed on WO_x films.[20] Recent work has also considered the role played by terminal oxo groups, M=O, which are common on both SiO_2 [42] and TiO_2 supported MO_x nanoparticles.[39]

Nonetheless, several critical issues remain largely unresolved. For instance, metal oxo species are of two types, monooxo M=O and dioxo O=M=O, and it remains unclear based on studies of high surface area catalysts if either or both are active for transformations such as alcohol dehydration? In addition it is unclear, what is the relative role of Brønsted acidity vs. Lewis acidity? How is acid/base chemistry and redox chemistry related in these materials? What is the fundamental chemical difference between the Mo and W sites, which leads to such different catalytic activity between these two oxides?

The focus of the current review will be to outline recent research activities based on model supported oxide clusters and films in ultrahigh vacuum (UHV) which have shed some light on these issues. A more general purpose review on a wider class of oxides was recently published by Stacchiola *et al.*,[31]

which briefly touches on these systems. However, the current review is more detailed focusing primarily on our own activities in understanding MO_3 based systems. The purpose of this review is to provide a focused discussion of what the authors believe are the key chemical properties of MO_3 which determine chemical reactivity and differentiates W and Mo.

The review is divided into five main sections. In Section 2, we focus on the structure and spectroscopic characterization of isolated $(WO_3)_3$ and $(MoO_3)_3$ clusters produced *via* sublimation of WO_3 and MoO_3 powders, respectively. In Section 3, we review the cluster chemistry in reactive matrices of alcohols and show that the primary differences between WO_3 and MoO_3 are a consequence of W^{6+} being the stronger Lewis acid and Mo^{6+} being the stronger oxidizing agent. In Section 4, we focus on the preparation and characterization on supported catalysts that are created by $(WO_3)_3$ deposition, and in Section 5, we review the catalytic activity of these materials in the dehydration, dehydrogenation and condensation of alcohols. Particular emphasis is placed on the role of monooxo and dioxo groups in controlling the reactivity and the role of metal oxide redox properties. The review concludes with Section 5 with an overall discussion of remaining challenges and controversies.

2. Isolated $(WO_3)_n$ and $(MoO_3)_3$ Clusters

2.1 Preparation of Cyclic $(WO_3)_n$ and $(MoO_3)_n$ Clusters

It has been demonstrated that polymeric species of tungsten and molybdenum trioxides, $(MO_3)_n$ (M = W, Mo), can be readily prepared in the gas phase *via* sublimation from their metal oxide solids.[43-45] As shown in mass spectrometry investigations,[45] the sublimation of WO_3 powder leads to a cluster distribution that is dominated by cyclic $(WO_3)_3$ trimers. The situation is more complex for MoO_3, where a broader distribution of cyclic clusters is observed and the cyclic $(MoO_3)_3$ represents only ~60% of the cluster size distribution.

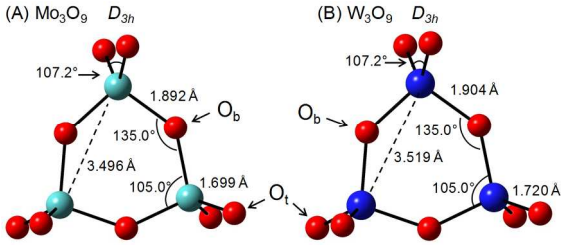

Fig. 1 Theoretically determined structure of cyclic $(WO_3)_3$ and $(MoO_3)_3$ clusters. Oxygen is red, molybdenum cyan, tungsten blue. Structures from Li and Dixon.[46]

Detailed spectroscopic studies (photoelectron spectroscopy (PES),[47, 48] infrared (IR) spectroscopy in the gas phase and inert matrixes,[49-55] mass spectrometry[46, 56]) combined with electronic structure calculations[46, 56] have led to the conclusion that both cyclic $(WO_3)_3$ and $(MoO_3)_3$ clusters are planar. As shown in Fig. 1, the cluster structures are nearly identical, with both having D_{3h} symmetry, each metal atom tetrahedrally coordinated with two bridging oxygen atoms (M-O-M, O_b), and two terminal oxygen atoms (M=O, O_t). Interestingly, these clusters have been highlighted as an example of d-orbital aromaticity due to the presence of fully delocalized d–d bonding interactions among the metal atoms.[48]

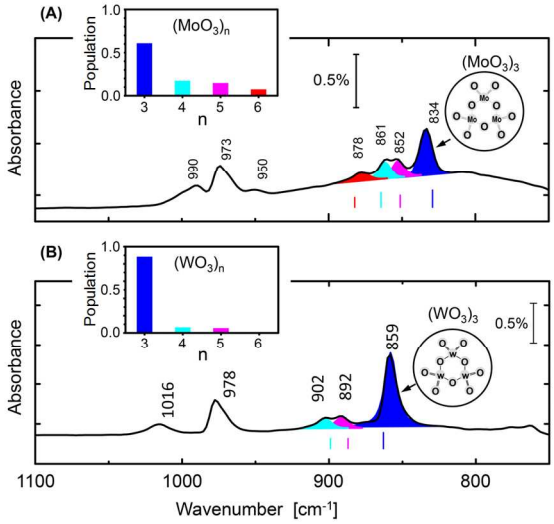

Fig. 2 Infrared reflection absorption spectroscopy (IRAS) spectra for (A) $(MoO_3)_n$ and (B) $(WO_3)_n$ suspended in a Kr matrix on an inert graphene substrate supported on Pt(111). Predicted vibrational frequencies[46] for different types of clusters are shown as "stick" spectra under the experimental peaks. The "stick" spectra for MoO_3 clusters were red-shifted by 29 cm^{-1} in order to match the experimental spectra. The insets show the population as a function of cluster sizes, *n*, as determined from the area of the M-O-M stretching mode peaks for various cluster sizes assuming identical oscillator strengths. Reprinted with permission from Li *et al.*[57]

The IR spectra for both WO_3 and MoO_3 clusters that were isolated in the Kr matrix are shown in Fig. 2.[57-59] Here the population of clusters of various sizes has been assigned by comparing the integrated intensities of various vibrational peaks as assigned from the theoretical studies of Li and Dixon.[46] Consistent with the expectations based on the cluster abundances observed in mass spectra,[45] the analysis yielded 89%, 6%, and 5% of cyclic $(WO_3)_3$, $(WO_3)_4$, and $(WO_3)_5$, respectively and 61%, 17%, 15% and 7% for cyclic $(MoO_3)_3$, $(MoO_3)_4$, $(MoO_3)_5$, and $(MoO_3)_6$, respectively.[57]

Confirmation that the metal centers in the intact clusters retain the (6+) oxidation state comes from X-ray photoelectron spectroscopy (XPS) measurements (Fig. 3) for clusters isolated in a matrix at low temperatures.[57] For W, this remains true even as the temperature is increased up to 600 K and the oxide clusters react with the alcohol matrix. Mo on the other hand, shows a tendency toward reduction to the (5+) oxidation state as the temperature is increased above 450 K.

2.2 Thermodynamic Properties of Isolated $(MO_3)_n$ Clusters

Much attention has been given to a careful quantification of the thermodynamic properties of $(MO_3)_n$ clusters. Recent advances in the scalability of parallel algorithms for computing high level correlated electronic structure methods, such as coupled cluster theories, have allowed for highly accurate computations of many chemical reaction energies associated with the gas phase oxide clusters.[60-63] Early work by Sun *et al.*[56] used density

functional theory (DFT) based methods for the calculations of both vertical and adiabatic electron affinities as well as fragmentation energies in order to interpret mass spectrometry data on WO_3 clusters. Later, Li and Dixon[46] extended this work to include structural, spectroscopic, and acid-base properties for $(MO_3)_n$ (M = Cr, Mo, W, n = 1 − 6) clusters. More recent computational studies at higher levels of theory have provided insights in the structure and energetics of negatively charged $(MO_3)_3^-$ anions, defect $W_3O_8^-$ clusters and hydroxylated species.[64-70]

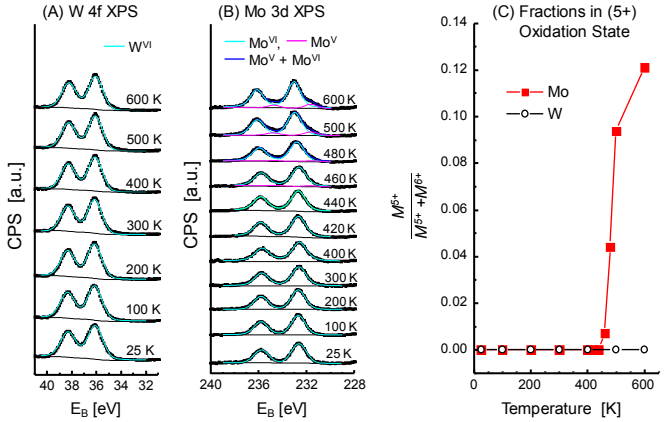

Fig. 3 (A) Binding energy, E_B, for W 4f levels determined using XPS. In the experiment, 2.0 × 10^{15} WO_3/cm^{-2} was co-deposited with 20 × 10^{15} CH_3CH_2OD/cm^{-2} on graphene/Pt(111) at 24 K and subsequently annealed to different temperatures. (B) E_B for Mo 3d levels for 2.0 × 10^{15} MoO_3/cm^{-2} co-deposited with 20 × 10^{15} CH_3CH_2OD/cm^{-2} on graphene/Pt(111) at 24 K and subsequently flashed to different temperatures. (C) Fractions of W and Mo reduced to the (5+) oxidation state as a function of temperature. Reprinted with permission from Li *et al.*[57]

For the purposes of the current discussion we will focus primarily on the most relevant thermodynamic properties that determine the reactivity of $(MO_3)_n$ clusters with organic species, namely, the Lewis and Brønsted acid/base and redox properties of the metal centers. The $(MO_3)_3$ clusters possess strongly Lewis acidic metal sites. For example, $(WO_3)_3$ has been computed to have a Lewis acidity of 117.9 kcal/mol (computed in terms of fluoride affinity at the CCSD(T) level) which is comparable to that of SbF_5.[69, 70] The Lewis acidity of $(MoO_3)_3$ is 105.3 kcal/mol which is smaller by about 10%.[69, 70] In addition, both O_b and O_t atoms are basic in nature. For example for $(WO_3)_3$, the O_t is found to be more basic than the O_b with corresponding gas phase proton affinities of 175.1 and 146.4 kcal/mol, respectively, at the CCSD(T) level.[69, 70] For $(MoO_3)_3$, similar energetics were computed with the gas phase proton affinities of 176.3 and 160.8 kcal/mol for O_t and O_b site, respectively.[69, 70] In general, O_b's exhibit appreciably lower proton affinities than O_t's for most gas phase clusters ($(MO_3)_n$, n = 2 - 6) except for isomers where the M-O-M angles are more constrained (e.g. low energy 3-dimensional $(MO_3)_6$). The implication of these observations is that for the smaller clusters, the preferred site for Lewis acid attack is the metal and for Brønsted acid attack is the O_t for both Mo and W clusters, with approximately the same Brønsted basicity. Conversely, although both Mo and W sites in these clusters are strongly acidic, W is clearly the stronger Lewis acid of the two.

To illustrate how these fundamental thermodynamic descriptors may influence chemical reactivity, we show in Fig. 4 how the H_2O adsorption and dissociation energies scale with fluoride affinity (Lewis acidity).[69, 70] From these correlations, which extend to a wider range of clusters than those discussed here, it can be clearly seen that weaker Lewis acidity leads to both a smaller desorption energy and lower stabilization energy for surface hydroxyls. Note that similar correlations have also been observed for fluoride affinities and proton transfer barriers in the same study.[69]

The reducibility of the metal center is also of fundamental importance as it affects redox reactions as further demonstrated below. This property can be calculated in terms of the adiabatic electron detachment energy (equivalent to the electron affinity of the neutral) as achieved for cyclic $(MO_3)_3^-$ anions at the coupled cluster level of theory by Li and Dixon.[66] For the cyclic $(MO_3)_3^-$ clusters which are similar to those of the neutral $(MO_3)_3$, values of 3.29 and 3.03 eV were obtained for Mo and W, respectively. The vertical electron affinity (VEA) for the cyclic $(MO_3)_3$ clusters had a larger difference of 0.54 eV derived from the VEAs of 2.52 and 1.98 eV for Mo and W, respectively. These results highlight a key difference between reactivity at W and Mo in that the Mo^{5+} is more stable relative to the Mo^{6+} by about 10 - 20% as compared with W^{5+} relative to W^{6+} (depending on the property of interest). The implications are that Mo is not only a mildly weaker Lewis acid but that it can be reduced easier (i.e. stronger oxidizing agent) than W to a lower oxidation state.

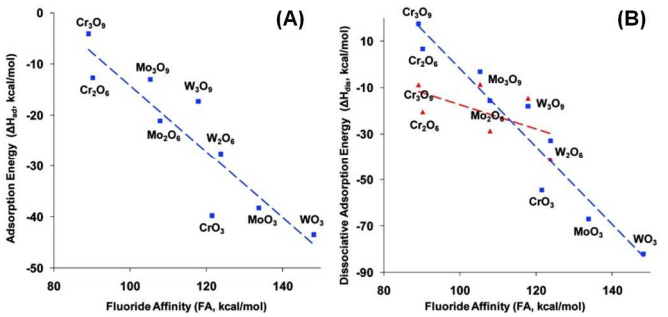

Fig. 4 Plots of (A) the H_2O adsorption energies and (B) the dissociative adsorption energies vs. the fluoride affinities (Lewis acidities). In (B), the dissociative adsorption energies for hydrogen transfer to the terminal M=O atoms are shown as blue squares, and those to the bridge M−O−M atoms are shown as red triangles. Reprinted with permission from Li *et al.*[69]

3. Reactions of Alcohols with Isolated $(WO_3)_3$ and $(MoO_3)_3$ Clusters

3.1 Ethanol Reactions with $(WO_3)_3$ and $(MoO_3)_3$ Clusters

As discussed above, direct sublimation of MoO_3 and WO_3 powders yields ensembles of clusters that are dominated by cyclic $(MO_3)_3$ trimers. When deposited at low temperatures into reactive matrices of organic molecules (here alcohols), one can directly probe their catalytic chemistry. Product formation can

be followed as a function of increasing temperature in temperature programmed desorption (TPD) studies, which in concert with *in situ* spectroscopic studies and theoretical simulations, can provide detailed quantification of the reaction energetics. This approach was first employed by our group for $(WO_3)_3$ in combination with complementary DFT simulations.[58, 71] More recently experiments were carried out for both $(MoO_3)_3$ and $(WO_3)_3$ clusters and compared with the energetics calculated using high level CCSD(T) simulations.[57]

The TPD results for deuterated ethanol (C_2H_5OD) are summarized in Fig. 5 where the product distributions were obtained for both $(WO_3)_3$ (upper black traces) and $(MoO_3)_3$ (lower red traces) clusters. The products shown in Fig. 5 are broken down into three types, (A) desorption of excess unreacted ethanol between 135 and 200 K, (B) evolution of water as the only observed carbon-free product and (C) evolution of carbon containing products.

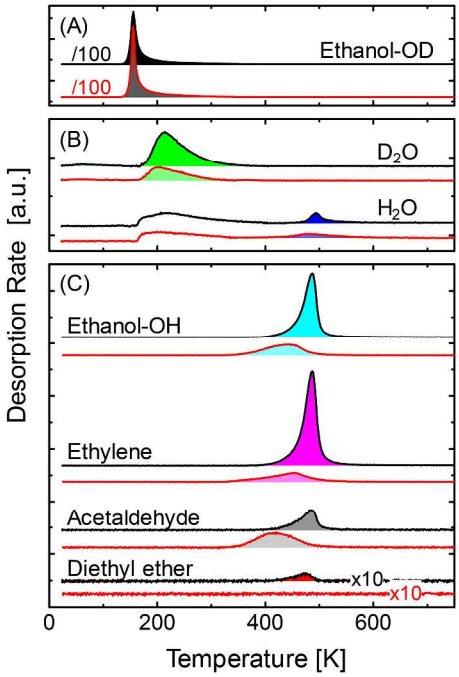

Fig. 5 Desorption rates of (A) CH_3CH_2OD, (B) D_2O and H_2O, and (C) CH_3CH_2OH, CH_2CH_2, CH_3CHO, and $(CH_3CH_2)_2O$ as a function of linearly increasing temperature (2 K/s) obtained during the TPD experiment following co-adsorption of 2.0×10^{15} WO_3/cm^{-2} (black) and MoO_3/cm^{-2} (red) with 20×10^{15} of CH_3CH_2OD/cm^{-2} on graphene/Pt(111) at 24 K. Reprinted with permission from Li *et al.*[57]

Focusing first on the evolution of the low temperature water, D_2O is observed between 170 and 300 K with a peak maximum between 200-220 K (Fig. 5B) on both $(WO_3)_3$ and $(MoO_3)_3$. The observation of D_2O indicates that a fraction of C_2H_5OD dissociated and that some deuterium was utilized to form D_2O. It has been concluded that water formation is a result of the deprotonation of alcohol molecules on the dioxo moieties of the clusters. The absence of H_2O indicates that C-H bonds are not being cleaved in this temperature range. Detailed quantitative analysis showed that on average ~0.56 D_2O molecules formed per W^{6+} center. On $(MoO_3)_3$, a significantly reduced yield of 0.21 D_2O/Mo^{6+} was observed.

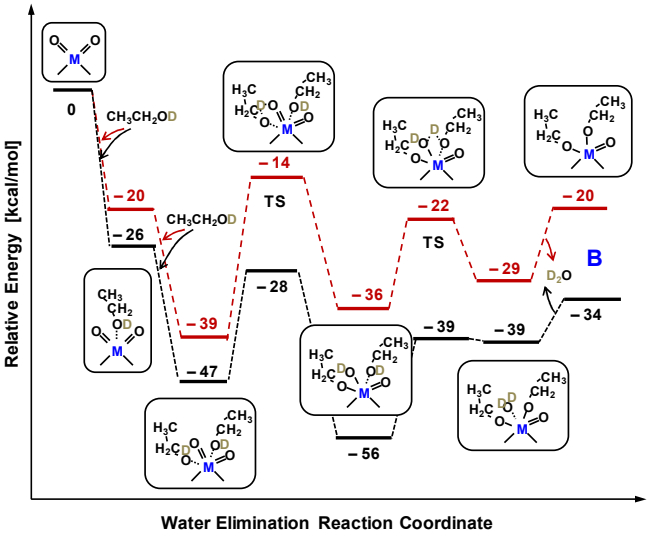

Fig. 6 CCSD(T) potential energy surface for the elimination of D_2O from the reaction of C_2H_5OD + $(MO_3)_3$, M = W, Mo. Energies in black are for W and in red for Mo. Reprinted with permission from Li *et al.*[57]

As the experiments were conducted in excess alcohol, the simulations were carried out by coordinating two alcohols per metal atom site as shown in the reaction schematic presented in Fig. 6. In accord with the higher Lewis acidity for W^{6+} discussed in the previous section, the well-depths are deeper for W than for Mo. Molecular adsorption is followed by two consecutive proton transfer steps to ultimately form two metal bound ethoxy species and a weakly coordinated D_2O. The weaker Lewis acidity of the Mo center manifests itself in multiple ways throughout the D_2O formation and desorption steps. First, the proton transfer barriers on the $(MoO_3)_3$ cluster are found to be slightly higher by about 4 kcal/mol than for the $(WO_3)_3$ analogue. Second, although the overall D_2O desorption energies of 19 and 22 kcal/mol from the most stable intermediates on $(MoO_3)_3$ and $(WO_3)_3$, respectively, are similar (hence similar desorption temperatures in TPD), they are chemically different. For the W cluster, the lowest energy structure along this path consists of W coordinated by ethoxy, hydroxy and a molecularly-bound alcohol. For Mo one finds the Lewis adduct structure with two ethanol molecules before proton transfers to be thermodynamically the most stable. The later thus implies that, water desorption is in a direct competition with ethanol desorption for Mo but not for W. This has led to the conclusion that the primary difference in the experimentally observed reactivity (almost three times lower on $(MoO_3)_3$) is linked to the higher Lewis acidity of W which stabilizes the initial complex and concomitantly lowers the proton transfer barrier. Note that desorption of this low temperature water has been found to be a critical step kinetically driving forward the formation of other organic products which are endothermic in overall reaction energy scheme.[58, 71]

In the final step of the conversion of ethanol-D, four major products are observed in the TPD at around 400 - 500 K, namely water, ethylene, acetaldehyde and non-deuterated ethanol as shown in Fig. 5B and C. These products arise from ethanol dehydration to H_2O and CH_2=CH_2, dehydrogenation to CH_3CHO, and desorption to CH_3CH_2OH with the caveat that the H atom bound to the hydroxyl group must have initially arisen from a C-H bond breaking process. The similar temperature range at which all of these reactions are observed implies that all three reaction channels are in competition and it is notable that the branching ratios show a pronounced difference for W vs. Mo. For the former, dehydration is the preferred channel whereas dehydrogenation is preferred for the latter. Comparative calculated reaction energetics for these two channels carried out at the CCSD(T) level are shown in Fig. 7 and Fig. 8. Dehydration on both W and Mo has a net overall reaction energy barrier of 35-36 kcal/mol which, as in the case of D_2O, would explain the similar desorption temperature observed in the TPD of Fig. 5. The transition state from this process has been postulated to involve the concerted breaking of the C_α-O and C_β-H bond and involves a carbo-cationic character to the C_2H_5 fragment.[58, 71]

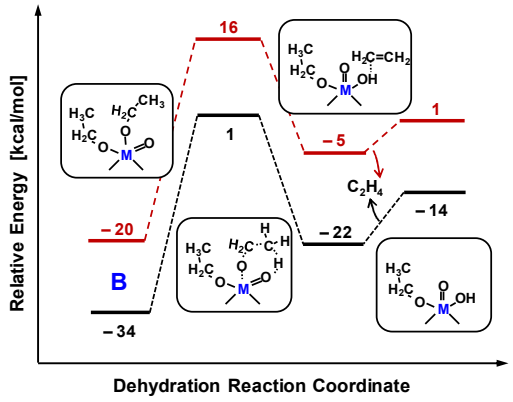

Fig. 7 CCSD(T) potential energy surface for the formation of C_2H_4 and the precursor state to releasing C_2H_5OH from the reaction of C_2H_5OD + $(MO_3)_3$. Reprinted with permission from Li *et al.*[57]

As a result, a proton is transferred back to the oxide cluster and can re-protonate any adsorbed ethoxy groups to ultimately release nondeuterated ethanol. Once a M=O bond is converted to a M-OH bond, a strong acid site is generated. As an example, the gas phase acidity of M_3O_8OH (OCH_2CH_3), formed after the addition of an alcohol by a proton transfer is 284.5 for Mo and 287.6 for W at the CCSD(T) level. These are much stronger gas phase acids than H_2SO_4 (304.0 kcal/mol).[72] Calculations indicate that the reprotonation of ethanol would have lower energy barriers than dehydration and thus can account for the observation of ethanol desorption at comparable temperatures as dehydration for both W and Mo. Conversely dehydrogenation shows an appreciably lower net reaction barrier for Mo and W; 34 and 43 kcal/mol, respectively. The proposed mechanism which involves heterolytic breaking of a C_α-H bond releasing a hydride species results in a transiently reduced metal center, which is in accord with the above discussion in more stable for the Mo cluster than the W analogue. As a result there is a marginally lower reaction energy for dehydrogenation on Mo than W and it thus becomes the dominant channel on $(MoO_3)_3$ clusters as opposed to the dehydration route observed on $(WO_3)_3$ clusters.

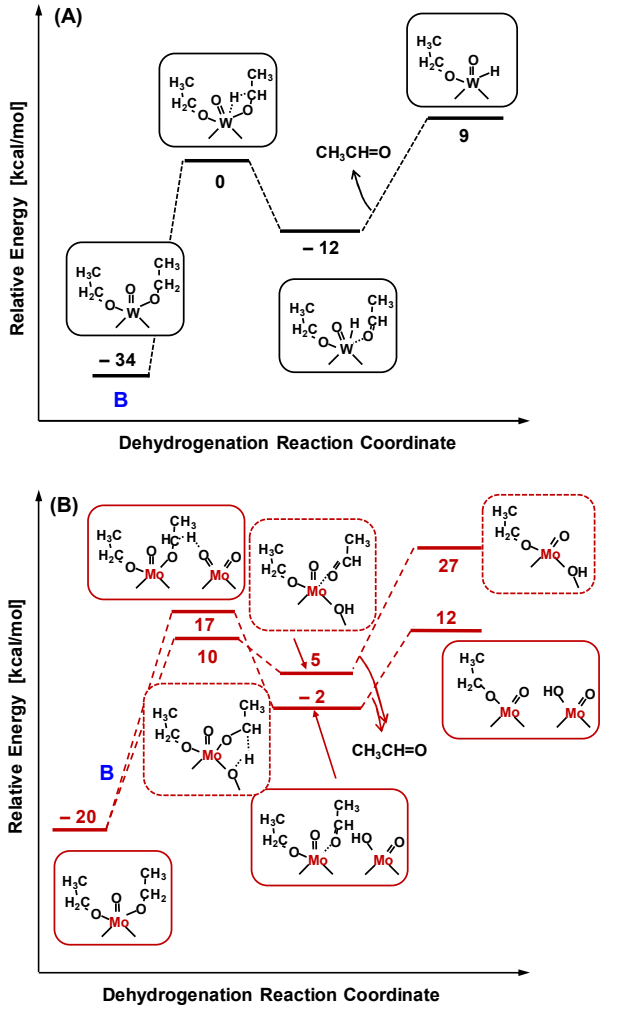

Fig. 8 CCSD(T) potential energy surface for the formation of $CH_3C(O)H$ from the reaction of C_2H_5OD + $(MO_3)_3$. Reprinted with permission from Li *et al.*[57]

A more direct comparison between theoretical and experimental observations is hampered by several complexities. First, it is clear that the clusters themselves are changing during the course of the experiment. As the temperature is increased and the matrix evaporates, the alcohol functionalized clusters can come into direct contact with each other. Second, computationally it has been observed that there are multiple, energetically similar pathways for all of the reactions described above. Nonetheless as already noted, the trends in the thermodynamic descriptors (Lewis acid and Basicity of the M=O groups and reducibility of the metal center) are relatively similar for various larger clusters.[46, 58, 66, 69-71, 73] The net result is that reaction energetics on sites of similar local chemical makeup are invariably similar within a few kcal/mol. (see

below for further discussion of this point). As a result the retention of active sites of a given type (e.g. monooxo vs. dioxo groups) is often sufficient to obtain reasonable estimates of reaction energetic barriers despite the fact that the underlying material one has compared with may have changed its overall morphology or cluster size substantially.

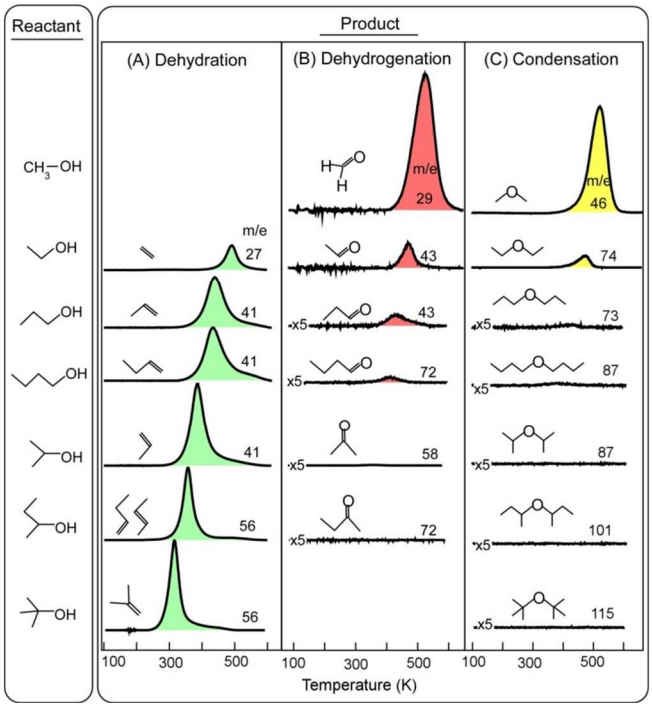

Fig. 9 TPD spectra of reaction products (alkenes, aldehydes, and dialkyl ethers) obtained from $(WO_3)_3$ clusters (1.1 nm^{-2}) deposited into a multilayer (24 molecules nm^{-2}) of C1 to C4 aliphatic alcohols at 100 K. Reprinted with permission from Kim *et al.*[58]

3.2 Trends in Reactivity with Primary, Secondary and Tertiary Aliphatic Alcohols

The underlying mechanisms for dehydration and dehydrogenation at the metal site have been further tested by examining the trends in reactivity across a series of aliphatic alcohols on $(WO_3)_3$ clusters.[58, 71] TPD spectra obtained from a reactive matrix of C1-C4 alcohols surrounding $(WO_3)_3$ clusters are presented in Fig. 9. In general, dehydrogenation and condensation has been observed to only be a significant path for primary alcohols and dehydration into alkanes is the dominant reaction channel for all species except methanol where this is not possible via the same mechanistic route. In accord with the stabilization of ionic transition states such as those formulated for the dehydration pathway, the reaction temperature decreases as alkyl chain lengthens and increases in branching from primary to secondary to tertiary alcohols. Moreover, this relationship is quantitative in that it has been shown that the apparent activation energy for the dehydration process scales linearly with the Taft inductive parameters[58, 74] consistent with the interpretation that the mechanism and reactive site for the entire series of alcohols is identical.

For dehydrogenation, a slightly different mechanism than the one in Fig. 9 was proposed based on DFT calculations that showed that C_α-H bond breaking resulted in a hydride transfer to a neighboring W site. The resulting intermediate however still involves a transiently reduced W^{4+} site, which is relatively high in energy. Based on this mechanism, the transition state is also partially ionic in nature, which would rationalize the observed decrease in activation energy with increasing alkyl group chain length by similar inductive arguments as proposed for dehydration.

It is also noted that a small percentage of diethyl ether is observed as a product. Although a mechanism based on DFT calculations has been proposed to involve the migration of an alkyl group between oxygen sites for this reaction channel[58] it remains to be seen if this mechanism will hold up to higher scrutiny in light of the fact that this relatively high energy mechanism must also compete with a Brønsted acid catalyzed mechanism involving the formation of protons liberated during the dehydration and the presence of three alcohol molecules.[41]

4. Supported Model Catalysts based on $(WO_3)_3$ Clusters

The accessibility of such simple and mostly monodispersed $(WO_3)_3$ and $(MoO_3)_3$ clusters affords an excellent opportunity to utilize them as building blocks in the preparation of well-defined supported model catalytic systems. These systems can in turn be used in model reactivity studies and yield valuable information about how the binding of such identical building blocks on different substrates can influence the activity. In this section we review structural studies that utilized the deposition of $(WO_3)_3$ on various metal and metal oxide substrates in the preparation of such model systems.

4.1 $(WO_3)_3$ Clusters Molecularly-bound on Striped Cu(110)-O

Intact, isolated $(WO_3)_3$ clusters were prepared on a Cu(110)-O stripe phase surface[75, 76] at 15 K and imaged at 5 K (Fig. 10) using high-resolution scanning tunnelling microscopy (STM). The coexisting bare Cu(110) and Cu(110)-(2×1)O regions that are illustrated in Fig. 10A, D allowed for simultaneous observation of the adsorption behaviour of $(WO_3)_3$ clusters on a surface with different types of chemical interactions and topographic corrugations.

On bare Cu(110), the clusters remained symmetric as shown by STM images obtained for a broad range of imaging voltages (3-0.6 V, Fig. 10B). DFT calculations further revealed that the bright spots in the images correspond to terminal, W=O oxygens that protrude above the ring plane. Interestingly, the fragmented image obtained at the lowest bias of 0.23 eV was interpreted (based on theoretical simulations) as being a result of the nodal structure of an unoccupied orbital located 0.35 eV above the Fermi level.

Spatially, two different configurations were observed relative to the underlying Cu(110) as schematically shown in Fig. 10D. The adsorption energy of the lowest energy configuration (Fig. 10D, top) was determined to be 6.47 eV

relative to gas phase cluster and clean Cu(110). In this configuration, the $(WO_3)_3$ cluster is bound via the three terminal W=O oxygen atoms below the ring plane to two parallel ridges of the Cu(110) surface occupying bridge sites between two vicinal Cu atoms. The second observed configuration (Fig. 10D, bottom) is simply shifted by a half period along a direction perpendicular to the surface ridges and, as shown by DFT, it is bound by 5.51 eV, which is 0.96 eV less than the top configuration.

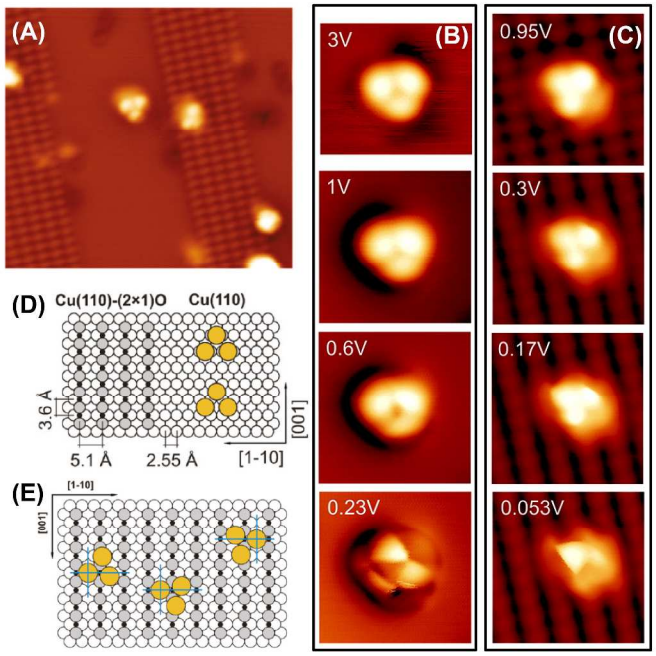

Fig. 10 STM images of the Cu-O stripe phase with $(WO_3)_3$ clusters deposited at 15 K and imaged at 5 K. (A) A large scale area (100 × 90 Å^2, 1 V, 0.1 nA) illustrating the alternating regions of bare Cu(110) and Cu(110)-(2×1)O regions. (B,C) High magnification STM images (25×25 Å^2, 0.1 nA) of $(WO_3)_3$ clusters as a function of sample bias on (B) Cu(110) and (C) Cu(110)-(2×1)O. (D,E) Schematics illustrating the adsorption sites of $(WO_3)_3$ clusters on (D) Cu(110) and (E) Cu(110)-(2×1)O. Adapted with permission from Wagner *et al.*[77]

In contrast with the $(WO_3)_3$ clusters on bare Cu(110), the clusters on Cu(110)-(2×1)O appear significantly distorted as seen in the STM images (Fig. 10A, C), likely due to the higher strength of the cluster/support interaction and Lewis acid interactions between tungsten and surface oxygen. Three out of four equivalent orientations that were experimentally observed are schematically shown in Fig. 10E. DFT studies have further revealed structural changes in both the cluster and surface structure and determined the binding energy to be 7.65 eV, which is 1.18 eV greater than on the bare Cu(110) regions. Additionally, an analysis of Löwdin charges showed that a substantial charge flow takes place from the oxidized metal surface to the oxide cluster.

It should be noted that these intact clusters that are observed at low temperatures will likely react further with the underlying Cu(110) and Cu(110)-(2×1)O substrates as the temperature is increased.

4.2 $(WO_3)_3$ Clusters Chemisorbed on Rutile TiO_2(110)

The formation of tight binding between $(WO_3)_3$ clusters and the underlying oxide substrate was clearly observed on rutile TiO_2(110). This substrate has achieved prototypical status as a reproducible single crystal of an early transition metal oxide surface that is amenable to studies in ultrahigh vacuum using electron-based methods, including atomically resolved scanning tunnelling microscopy.[78-80] As such, TiO_2(110) was naturally selected as a substrate for the deposition of gas phase $(WO_3)_3$ clusters.[81, 82] The TiO_2(110) is a corrugated substrate with topographically low-lying rows of pentacoordinated titanium (Ti_{5c}) ions and high-lying rows of bridge-bonded oxygen (O_b) ions as illustrated in Fig. 11.[78-80]

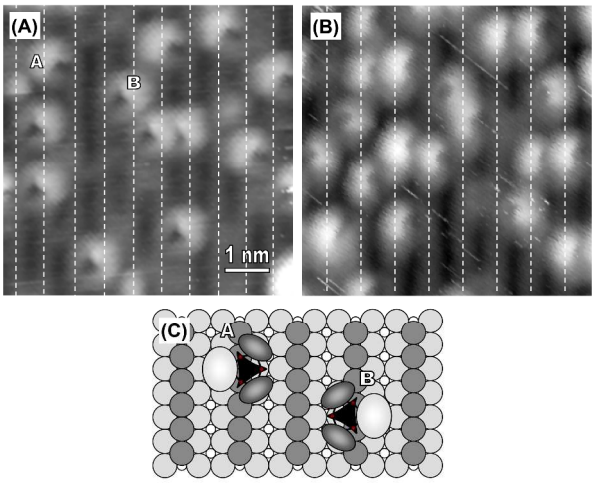

Fig. 11 (A, B) High-resolution empty-state STM image (70 × 70 Å) of isolated $(WO_3)_3$ nanoclusters following the $(WO_3)_3$ deposition at 300 K and annealing to 600 K. The dashed lines mark the positions of the titanium rows that are separated by 6.5 Å. (C) Schematic of the proposed geometry of tilted cyclic $(WO_3)_3$ adsorbed on TiO_2(110). Surface oxygen ions are grey (dark – bridging O, light – in plane O), titanium ions are white. Adapted with permission from Kim *et al.*[82]

The images of WO_3 adsorbates obtained after the deposition at 300 K (not shown) exhibited only dark unresolved regions on the bright Ti_{5c} rows indicating the presence of deposited $(WO_3)_3$. The dark regions typically involved at least two neighbouring Ti_{5c} sites and within the rows extended over distances of at least two Ti_{5c} sites. While these images did not allow for direct identification of individual clusters, subsequent annealing to 450 - 600 K led to well-resolved $(WO_3)_3$–related features as illustrated in the high resolution images shown in Fig. 11a-b. These images are dominated by very bright isolated features that have a crescent-like shape. The alternating bright and dark rows of low-and high-lying titanium and bridging oxygen rows, respectively, of the underlying TiO_2(110) surface can be also recognized. The observed cluster images varied slightly depending on the specific tip conditions[81, 82] but in most cases their shape was round and lacked the crescent like appearance. From the coverage dependent analysis, it was concluded that most clusters are centred on Ti_{5c} rows with a small fraction (~20 %) centred on a bridging oxygen row. It was speculated that the minority bridging oxygen row centred

clusters are bound to bridging oxygen vacancy sites. The number of observed features was correlated with the total deposited WO_3 mass as determined by a quartz crystal microbalance (QCM) and showed clearly that each bright feature contains three WO_3 units supporting the arguments for cyclic $(WO_3)_3$.

Complementary XPS studies further demonstrated the high thermal stability of the WO_3 deposits with respect to reduction up to ~750 K. A small amount of reduction of W^{6+} to W^{5+} was revealed by W_{4f} spectra above this temperature. Additionally, the fact that the integral of the W_{4f} spectra did not change between 300 and 900 K indicated the lack of WO_3 diffusion into bulk TiO_2(110).

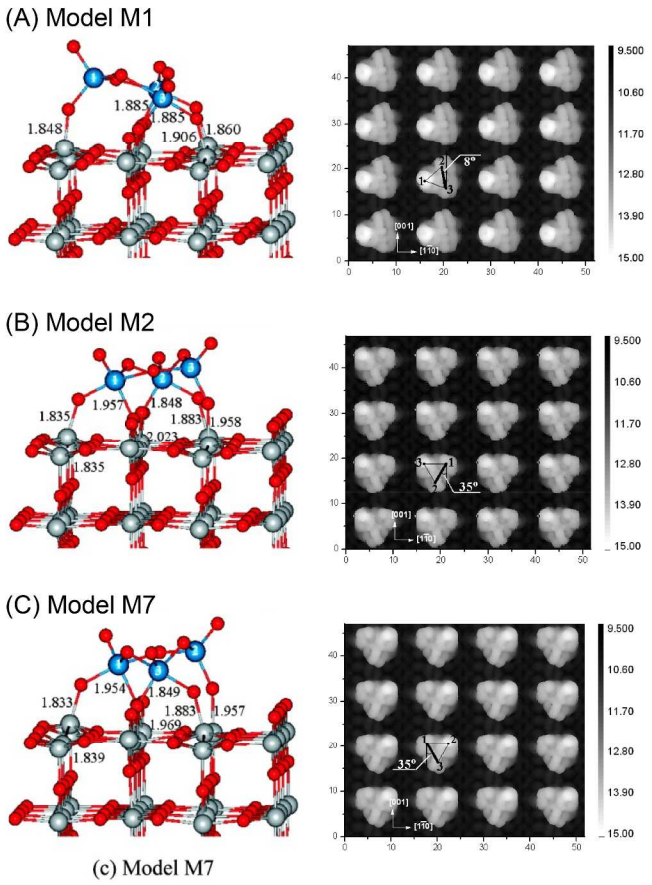

Fig. 12 Left: Optimized structures of three thermodynamically preferred models for the $(WO_3)_3/TiO_2$(110). The W, O, and Ti atoms are denoted by blue, red, and grey spheres, respectively. Right: Simulated STM images under empty state imaging conditions (V = +1.7 V). The positions of the three tungsten atoms of the $(WO_3)_3$ clusters are denoted by the vertexes of the triangle, and the edge opposite to the highest W atom is indicated by a thick line. The deviation angle between this edge and the Ti_{5c} and O_b row direction (running vertically) is also given. The values shown in all panels are in Angstroms. Adapted with permission from Zhu *et al.*[83]

Only a simplistic explanation of the cluster binding was initially put forward based on the observations in these experimental studies.[81, 82] The atomistic structure of the $(WO_3)_3/TiO_2$(110) system was subsequently explored in great detail in independent theoretical studies.[83-86] In the first study Zhu *et al.* explored possible $(WO_3)_3$ configurations and electronic structures on a stoichiometric TiO_2(110) (no surface oxygen vacancies and excess charge) by first screening the potential structures using DFT based *ab initio* molecular dynamics (AIMD) and subsequently optimizing stable configurations by quenching structures to T = 0 K from these trajectories.

The most stable configurations, Fig. 12 (left), were found to be bound by three O_t atoms of the cluster to the titanium sites and two additional bonds between W and surface bridging oxygens. Two of the most stable models, M2 and M7, are almost identical as they have the same adsorption pattern and can be viewed as chiral isomers. The M1 structure was found to have the highest adsorption energy of 4.34 eV and to be only slightly negatively charged (-0.06 e). Both the M2 and M7 models have similar charge (-0.08 e) but slightly lower adsorption energy (4.12 eV) than the M1 model. Interestingly, they were observed more frequently in the AIMD simulations.

To further compare the results of the simulations with the STM experiments (see Fig. 11), Zhu et al. used the Tersoff-Hamann approximation and simulated empty state images for their most stable structures (Fig. 12, right). The brightest features in the simulated STM images were determined to originate primarily from the 5d states of W^{6+} ions. While the study favoured the M2 and M7 configurations as they appeared more often in the simulations, the lowest energy configuration M1 seems also plausible and may agree better with the STM images shown in Fig. 11.

Subsequent DFT studies by Di Valentin *et al.* explored $(WO_3)_3$ adsorption on both stoichiometric and reduced TiO_2(110) surfaces.[86] The results on stoichiometric TiO_2(110) were consistent with the previous study by Zhu et al.[83] and the authors further emphasized that the interactions between the clusters and the surface can be described in terms of Lewis acid/base interactions with electrons being donated from basic O_t to acidic surface titanium and from acidic W^{6+} to basic surface bridging oxygen sites.

Interestingly, the $(WO_3)_3$ adsorption energy on the bridging oxygen defects of reduced TiO_2(110) was found to be significantly smaller than that on stoichiometric surface (2.2 *vs.* 3.2 eV) for both singlet and triplet configurations.[86] Only three bonds formed in this case, one of the O_t ions fills the bridging oxygen vacancy and two additional O_t atoms interact with two surface titanium ions (not shown).

4.3 Dissociated $(WO_3)_3$ on FeO(111)/Pt(111)

Further progression in the strength of the $(WO_3)_3$ interactions with various substrates can be seen on FeO(111) thin film on Pt(111). Here the clusters were found to dissociate to their monomeric WO_3 units. This was extremely surprising as the FeO(111) substrate was heuristically expected to be rather inert due to its oxygen termination.

Monolayer thick FeO(111) films grown on Pt(111) have been employed in numerous studies both as active catalysts and as supports for metal clusters.[87-89] The film is composed of a FeO(100) bilayer with oxygen ions forming the outer layer as

shown in the schematics presented in Fig. 13. Due to the lattice mismatch between FeO(111) and Pt(111), a hexagonal moiré pattern (bright and dark areas) is formed as clearly visible in the high resolution STM images shown in Fig. 13A, B. While initially thought to be fairly inert as a result of oxygen termination, later studies showed that the films are highly active and can oxidize, hydroxylate, and/or dewet at higher reactant pressures[90-92] and that the FeO island edge sites can be highly catalytically active (e.g. for CO and alcohol oxidation).[93-95]

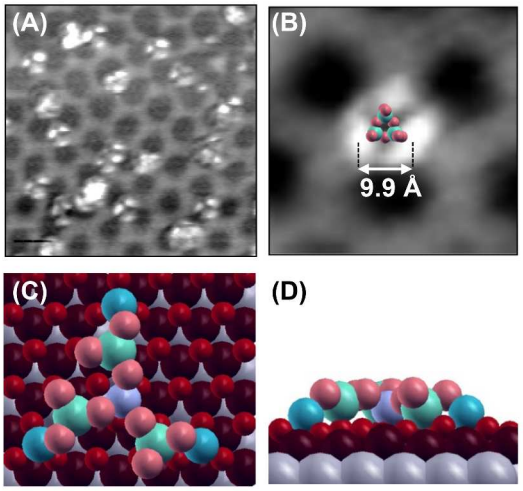

Fig. 13 Empty state STM images of FeO(111) after the deposition of 2 × 10^{13} WO_3/cm^2 (this corresponds to 6 × 10^{12} $(WO_3)_3$ $/cm^2$) at 300 K. Image sizes: (A) 15×15 nm^2 and (B) 4 × 4 nm^2. Image (B) is overlaid with a model of the cyclic gas-phase $(WO_3)_3$ cluster. (C) Top and (D) side view of theoretically predicted structure following $(WO_3)_3$ adsorption on FeO(1110) and its dissociation into three monomeric WO_3 units. Pt - grey, Fe - dark red, W - green, O from FeO - red, O from WO_3 - light red. Adapted with permission from Li *et al.*[96]

Also, studies of $(WO_3)_3$ on FeO(111) have demonstrated that the highly oxophilic Fe^{2+} ions interact strongly with electron rich W=O bonds of the clusters.[96] An image following $(WO_3)_3$ deposition on FeO(111) at 300 K is shown in Fig. 11A. Most of the clusters appear triangular with three bright lobes cantered on the bright underlying *top* and *hcp* FeO(111) areas ~70%). The preference for $(WO_3)_3$ adsorption on the bright FeO(111) areas can be understood in terms of the tendency to donate charge (e.g., from oxygen lone pairs) to the slightly charge-depleted (bright) *top* and *hcp* sites.[97] A detailed image in Fig. 13B further shows that the distances between the bright spot maxima are significantly larger, ~10 Å than then the W–W and O_t–O_t distances of 3.52 and 5.19 Å in the cyclic gas phase $(WO_3)_3$ cluster (see Section 2). Based upon these observations it was concluded that the clusters are dissociated. This conclusion is also supported by the lack of any changes upon annealing up to 800 K and the presence of some irregularly shaped features that can be seen in Fig. 13A. The XPS studies further showed that W remains in (6+) oxidation state between 300 and 800 K and the infrared reflection absorption spectroscopy (IRAS) spectra exhibited a broad mostly unchanged feature at 1020 cm^{-1} interpreted as being due to W=O stretching mode.[88, 98]

The viability of the $(WO_3)_3$ dissociation was further ascertained *via* DFT calculations. While a simple dissociation on structurally-static FeO(111) was shown not to be viable, when concurrent rearrangements within the FeO(111) overlayer were allowed, a highly exothermic (~340 kJ/mol) dissociation path leading to monomeric WO_3 fragments was found (see Fig. 13C, D). The calculations have shown that $(WO_3)_3$ dissociates in a stepwise fashion, starting with the initial ring opening (barrier 51 kJ/mol), followed by subsequent break-up of the cluster into WO_3 units (barriers 73 and 78 kJ/mol). During this break-up the Fe ions are being pulled to the top of the FeO(111) layer, thereby facilitating dissociation and enhancing WO_3 bonding. The W ions in the WO_3 fragments were found to remain in the (6+) oxidation state and to have a single W=O group.

4.4 Charged $(WO_3)_3$ Clusters on MgO(001)

While no experimental studies of $(WO_3)_3$ on MgO(001) are available at present, an interesting theoretical study[99] predicted how the structure and charge of the $(WO_3)_3$ clusters will change with the proximity of the metal substrate (e.g. Ag(001)) that the MgO(001) films are grown on.

Thin oxide MgO(001) films that can be prepared with smoothly varying thickness ranging from a few layers to a bulk-like limit have proven to be an extremely valuable in the understanding of the role of charge in the structure and properties of supported species.[88, 98, 100-102] While charge transfer through thick insulating films is not possible, charge tunnelling occurs readily through films that are generally thinner than ~ 1 nm. Specifically, it has been shown that ultrathin films allow for spontaneous charge transfer from the metal support to an adsorbed atom, molecule, or metal nanoparticle (or vice versa). This has been demonstrated for Au atoms and clusters,[88, 98, 100, 101, 103-107] as well as simple molecules such as O_2 [108, 109] and NO_2 [110] on two to three layer thick MgO(001) films on Ag(001).

Analogous charge transfer effects have been explored theoretically for $(WO_3)_3$.[99, 111] The results of these first principles DFT MD simulations showed dramatic differences (Fig. 14) between the structure and charge of the $(WO_3)_3$ supported on ultrathin MgO(001)/Ag(001) and on bulk MgO(001).

While on bulk MgO(001) the $(WO_3)_3$ clusters remained cyclic, they were found to distort significantly from their gas phase structure as illustrated in the schematics presented in Fig. 14a. The clusters were found to bind with four terminal O_t atoms and one bridging O_b to Mg^{2+} surface ions *via* dative bonds and at the same time with two W^{6+} ions to surface O^{2-} ions. The binding energy corresponding to this configuration was determined to be 2.98 eV. The clusters were found to be negatively charged, $(WO_3)_3^{1-}$, (0.85 e transferred to the cluster) primarily as a result of the interactions of surface O^{2-} with W ions.

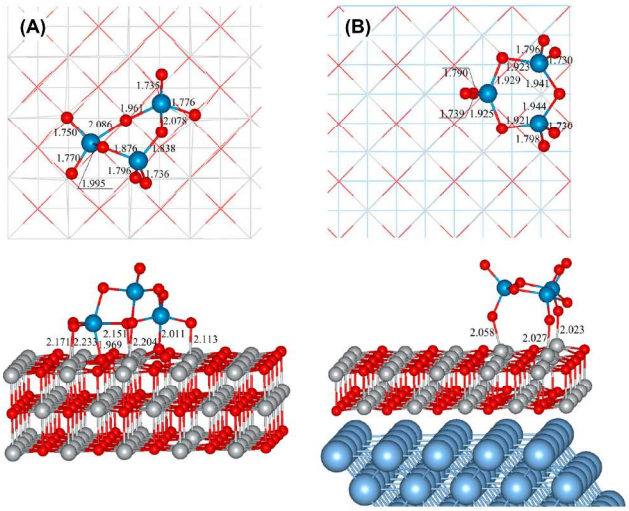

Fig. 14 Optimized ground state structures of (A) $(WO_3)_3$/MgO(001) and (B) $(WO_3)_3$/MgO/Ag(001) (top and side views). W, O, Mg, and Ag atoms are denoted by dark blue, red, grey, and light blue spheres, respectively. Selected bond lengths are given in Å. Reprinted with permission from Zhu *et al.*[99]

In contrast with bulk MgO(001), on ultrathin MgO(001)/Ag(001), the clusters were found to mostly maintain their symmetric cyclic structure. Only three bonds are formed, via three terminal O_t's of the cluster to surface Mg^{2+} ions without any direct bond between W^{6+} ions and the surface O^{2-} ions. The clusters are bound more tightly (3.48 eV) than on bulk MgO(001) and are doubly negatively charged, $(WO_3)_3^{2-}$. The two extra electrons were found to originate directly from the Ag substrate.

The differences in the $(WO_3)_3$ cluster structure and properties in these two limits should be distinguishable not only based on their different appearance in STM images but also based on their electronic and vibrational spectroscopic signatures.[99] As such they represent an excellent model system for future experimental explorations, both in terms of structure characterization and catalytic activity.

4.5 Ordered $(WO_3)_3$ Films on Pt(111)

While intact clusters can be prepared on metal surfaces at low temperatures as illustrated by $(WO_3)_3$ on Cu(110).[77] In most cases, the strong interactions between the W=O groups of the clusters will provide a strong thermodynamic driving force for structural rearrangements and possible reduction. This can be illustrated for $(WO_3)_3$ deposited on Pt(111) at elevated temperatures (600 – 800 K) where the kinetic hindrances toward achieving thermodynamically stable structures can be overcome.

Low energy electron diffraction (LEED), XPS, IRAS, and STM techniques were employed to obtain a comprehensive characterization of the WO_3 films and provided input for DFT calculations that were used to determine the film structure.[59] Based on the combined evidence, the first WO_3 layer (Fig. 15A, top) that is in direct contact with Pt(111) was found to nucleate along the step edges, be partially reduced (50% of W atoms are in (+5) oxidation state), and have a c(4×2) periodicity. DFT calculations revealed that cluster adsorption is followed by ring opening and polymerization into chain like-structures that can further assemble into a complete layer (Fig. 15A, bottom) at a coverage of 0.5 WO_3 per surface Pt. The overall energetics of this film formation sequence is exothermic by 1.39 eV per WO_3 with respect to gas phase $(WO_3)_3$ and clean Pt(111) and by 0.57 eV relative to chemisorbed cyclic $(WO_3)_3$.

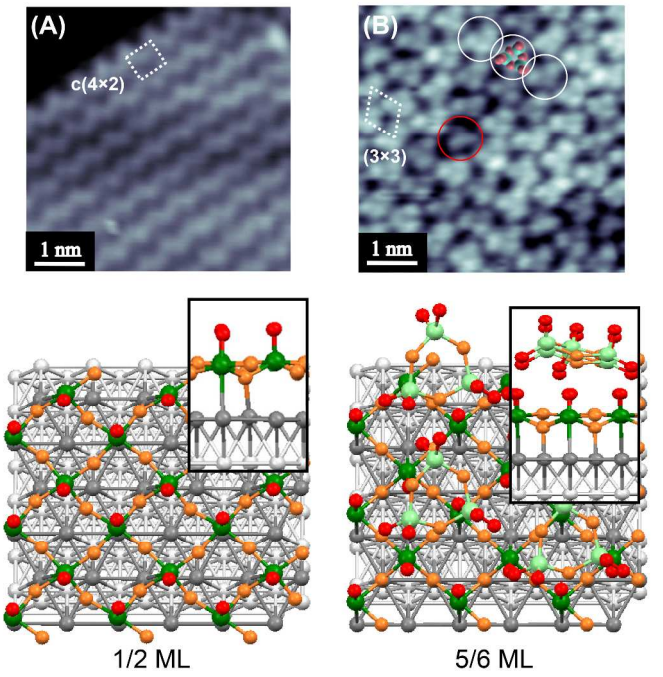

Fig. 15 STM images and corresponding structures from DFT calculations determined for one (A) and two (B) layer thick films resulting from $(WO_3)_3$ deposition on Pt(111) at 700 K. The dotted lines mark the c(4×2) and (3×3) unit cells. White circles in (B) mark several $(WO_3)_3$ trimers as building block of the (3×3) overlayer, one overlaid with the trimer structure. The red circle marks a $(WO_3)_3$ defect cluster that is rotated by 180° with respect to the rest of the $(WO_3)_3$ trimers. Legend for the theoretically determined structures: Pt grey, W in first (second) layer dark (light) green, O in W=O (W-O-W) groups red (orange). Adapted with permission from Li *et al.*[59]

As the WO_3 coverage was increased, the onset of second layer nucleation preceded completion of the first layer indicating comparable thermodynamic stability of the two layers. Characterization of the second layer showed that it is composed of intact $(WO_3)_3$ trimers laying with their rings flat and arranged in a (3×3) overlayer relative to the underlying Pt(111). This can be seen in the STM image displayed in Fig. 15B. The three-spot motif due to the structure of the $(WO_3)_3$ trimers is highlighted by several white circles on the image. An example of the defect in the structure that is a result of one of the $(WO_3)_3$ being rotated by 180° along the surface normal with respect to other clusters is highlighted by a red circle. Theoretical studies further confirmed that the nucleation of the second layer is highly favoured and that the overall energy of the two layer film is (total coverage of 5/6 WO_3 per Pt) comparable (1.17 eV per WO_3) with that of the single layer film.

4.6 Nanoporous WO_3 Films

Preparation of well-defined, high surface area materials under controlled UHV conditions is generally not a straightforward task. Ballistic deposition is a novel method that can be employed for the growth of supported nanoporous films of various materials.[112-125] Such films can be subsequently used in reactivity studies providing complementary information about the activity of low coordinated sites thereby facilitating direct comparison with the results obtained on single crystals and/or epitaxial thin films.

While the growth of ordered thin films generally relies on fast surface diffusion of the deposited species at high substrate temperatures, the growth of porous films via ballistic deposition requires limited surface diffusion and therefore is normally carried out at low substrate temperatures. Under such conditions the species impinging from the vapour phase are incorporated at and/or very near the site where they initially land (hit and stick).[112, 113, 115, 116] Because of the random nature of the deposition process, higher and lower areas develop. The asperities preferentially capture the incoming flux, while the regions behind are shadowed. The length of the shadows increases proportionally with the tangent of the incident angle which becomes very large at grazing incidence angles leading to the formation of columnar, porous films. Films with extremely high surface areas can be grown using this techniques.[114, 118, 120, 121, 126]

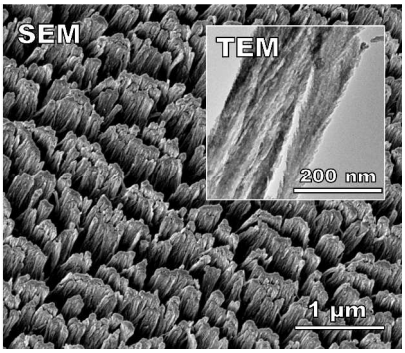

Fig. 16 SEM and TEM images of a nanoporous WO_3 film deposited at an incident angle of 85° and a substrate temperature of 20 K. The amount of deposited WO_3 corresponds to 100 ML of dense WO_3. Reprinted with permission from Li *et al.*[73]

The morphology of a nanoporous WO_3 film grown by depositing $(WO_3)_3$ on a graphene monolayer on Pt(111) at 20 K at 85º incidence angle is shown in Fig. 16. The filamentous structure of the film is readily apparent in the scanning electron microscopy (SEM) image. A more detailed view of several individual filaments is further shown in the transmission electron microscopy (TEM) image (Fig. 16, insert). The X-ray diffraction (XRD) and secondary electron diffraction (SED) showed that the "as-grown" films have an amorphous structure while adsorption measurements revealed that the films possess surface areas as high as 560 m^2/g. This is at least an order of magnitude higher than any previously reported specific surface area for WO_3 powders.[127] The annealing-dependent changes in the film morphology are further discussed in the Section 5.2 as the observations are directly relevant to their catalytic activity.

5. Reactions of Alcohols on $(WO_3)_3$-based Supported Model Catalysts

5.1 Reactivity of $(WO_3)_3$ Clusters Supported on Other Oxides

As discussed in the previous section, the STM studies of $(WO_3)_3$ deposited on $TiO_2(110)$ show dramatic changes in the cluster appearance with annealing temperature. Similarly, significant changes were also observed in the $(WO_3)_3$ reactivity with small aliphatic alcohols. This is illustrated in Fig. 17 where reactivity with 2-propanol was assessed in terms of propene formation in TPD experiments on $(WO_3)_3$ clusters prepared under different conditions. In Fig. 17A, the $(WO_3)_3$ clusters were deposited on top of 2-propanol multilayers on $TiO_2(110)$ as illustrated in the corresponding schematic. This experiment aimed to model the reactivity of unsupported, isolated $(WO_3)_3$ clusters which is discussed in detail in Section 3.

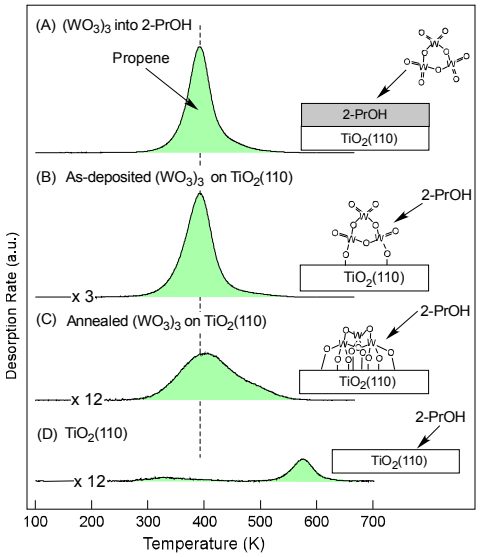

Fig. 17 Propene TPD spectra (tracked at 41 amu) resulting from 2-propanol dehydration on $(WO_3)_3$ clusters. (A) $(WO_3)_3$ cluster are deposited into multilayers of 2-propanol (18 nm^{-2}) on $TiO_2(110)$; (B) $(WO_3)_3$ clusters are deposited onto $TiO_2(110)$ at 100 K and subsequently exposed to 2-propanol (18 nm^{-2}); (C) clusters from (B) are annealed to 600 K and exposed to 18 nm^{-2} of 2-propanol; (D) dehydration of 15 nm^{-2} of 2-propanol on clean $TiO_2(110)$ is also shown for comparison. [74, 128, 129] The schematics are only simple illustrations of what was envisioned happening with the clusters vs. annealing temperatures. Reprinted with permission from Kim *et al.* [129]

In Fig. 17B, the clusters were deposited onto $TiO_2(110)$ at 100 K and subsequently exposed to excess 2-propanol. This scenario likely corresponds to $(WO_3)_3$ clusters that in STM images showed only a fuzzy appearance, which is indicative of their mobility and rather weak binding.[81, 82] In Fig. 17C, the clusters prepared in Fig. 17B were further annealed to 600 K before exposure to 2-propanol. This corresponds to the fully bonded $(WO_3)_3$ clusters that are shown in the STM images presented in Fig. 11. A propene TPD spectrum from 2-propanol

dehydration on clean TiO_2(110) is also included (Fig. 17D) for comparison.[74, 128, 129]

Surprisingly, the $(WO_3)_3$ deposition method (and consequently cluster/substrate binding) did not affect the propene formation temperature as indicated by the identical desorption temperature for all three cases (Fig. 17A-C). This indicates that the activation energy for dehydration is unaffected by the cluster proximity and/or binding to TiO_2(110). The only difference among the desorption traces, is a small broadening of the desorption peak that occurs from spectrum A to B with the appearance of an additional high temperature shoulder (~480 K) on spectrum in Fig. 17C. Interestingly, the dehydration channel observed on TiO_2(110) at ~570 K is completely suppressed.

Further demonstration of the sustained catalytic activity of the $(WO_3)_3$ clusters on TiO_2(110) is revealed in the reactive scattering experiments illustrated in Fig. 18. While TPD experiments clearly demonstrated the ability of supported $(WO_3)_3$ clusters to dehydrate alcohols to alkenes, the reactive scattering experiments show that the reactions can be sustained over extended periods of time. Time dependent waveforms of propene formation at 300 and 450 K on $(WO_3)_3/TiO_2$(110) prepared at 300 K are shown in Fig. 18A. While no propene is observed at 300 K, sustained propene formation can be seen at 450 K demonstrating stability of the catalyst. The increase of the propene yield with increasing temperature is further shown in Fig. 18B.

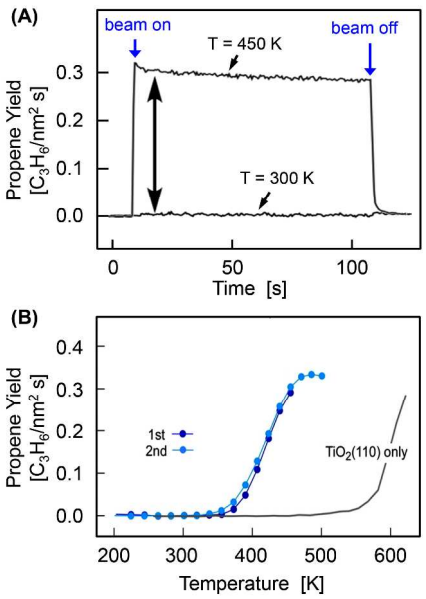

Fig. 18 Reactive scattering of 2-propanol from $(WO_3)_3/TiO_2$(110) catalyst (0.6 $(WO_3)_3/nm^{-2}$ deposited at 300 K) demonstrates sustained propene formation. (A) Time dependent propene signals obtained at 300 and 450 K. (B) Propene yield as a function of $(WO_3)_3/TiO_2$(110) temperature. Identical waveforms for first and second run illustrate catalyst stability to ~450 K. Propene yield from bare TiO_2(110) is provided for a reference. Previously unpublished data.

The TPD spectra in Fig. 17 show a large decrease in propene yield going from 17A to 17C (note the scale factors). The observed decrease in the propene yield was assessed in terms of decreasing number of available W=O species as the temperature is increased and the clusters bind strongly with the underlying TiO_2(110). This is supported by DFT calculations[83, 86] which are discussed in Section 3 in the context of matrix isolation experiments. We further address this issue in the next section.

Analogous to the 600 K annealed $(WO_3)_3$ clusters on TiO_2(110) (Fig. 17C), the dehydration yield of 2-propanol on the dissociated $(WO_3)_3$ clusters on FeO(111)/Pt(111) (see Section 4.3, Fig. 13 for the structure) is very low.[96] This is illustrated in the TPD spectra following the 2-propanol adsorption shown in Fig. 19. Interestingly, the small amount of propene that is observed shows a maximum at 419 K, a temperature that is practically identical with that observed on $(WO_3)_3$ on TiO_2(110) further indicating that the substrates do not significantly influence the energetics of the dehydration reaction.

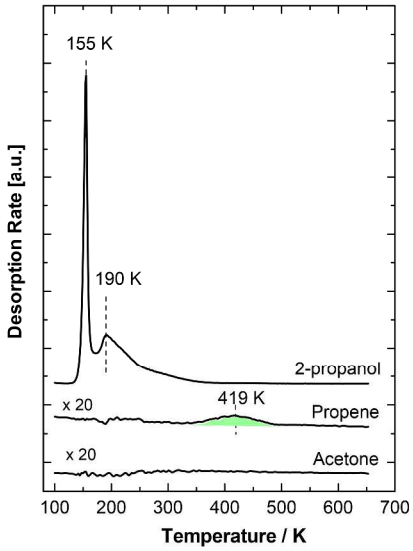

Fig. 19 TPD spectra of 2-propanol, propene, and acetone following the 1.0×10^{15} cm^{-2} dose of 2-propanol on 2×10^{14} WO_3/cm^2 on FeO(111). Reprinted with permission from Li *et al.*[96]

5.2 1-Propanol on Nanoporous WO_3

While the experimental and theoretical evidence obtained from the reactivity studies on unsupported $(WO_3)_3$ clusters and $(WO_3)_3$ supported on TiO_2(110) and FeO(111) was highly suggestive of the importance of the presence of dioxo O=W=O species,[57, 58, 71, 96] further evidence for this assertion was obtained from the alcohol reactivity studies on nanoporous WO_3 films prepared by ballistic deposition of $(WO_3)_3$ (see Section 4.6 for preparation and structure).[73, 126]

In these experiments, the surface area, integrated W=O stretching band, and propene formation by 1-propanol dehydration were measured as a function of the WO_3 film annealing temperature. As can be expected, the surface area (determined from TPD of Kr monolayer) decreased with increasing annealing temperature as illustrated in Fig. 20 (circles). Interestingly, the integrated W=O stretching band

(triangles) which here represents the sum of both monooxo and dioxo species decreased in the same fashion as the film surface area. In contrast, the propene yield (squares) decreased significantly faster than the sum of the monooxo and dioxo species. The faster decrease in the reactivity as compared with the surface area or the intensity of the W=O stretch was hypothesized to result from the thermal conversion of dioxo species (dehydration active) to monooxo species (dehydration inactive), as schematically shown below:

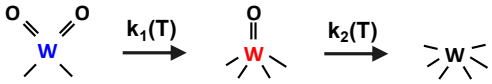

A simple kinetic analysis of the experimental data assuming that the annealing driven annihilation of W=O bonds for both dioxo and monooxo species follows the same kinetics fit the experimental data and further supported this conclusion.[73]

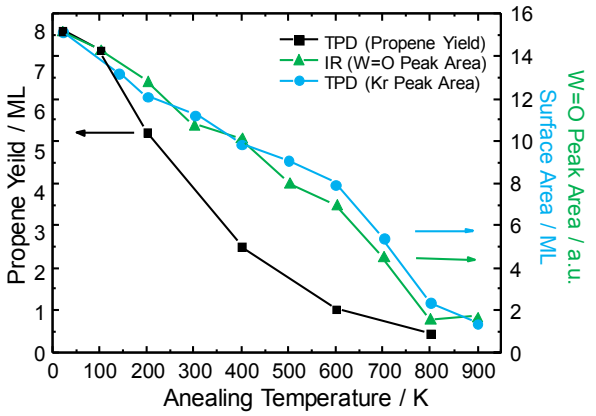

Fig. 20 Surface area from Kr monolayer TPD (blue), integrated W=O stretching band from IRAS (green), and propene yield from propene TPD (black) following 1-propanol adsorption on nanoporous WO_3 film (10 ML dense WO_3 equivalent, deposited at 20 K and 65° incidence angle) as a function of film annealing temperature. Krypton and propene TPD peak areas are normalized relative to their monolayer peak areas on Pt(111). Adapted with permission from Li *et al.*[73]

The energetics of the dehydration on the monooxo and dioxo groups of the nanoporous films was further addressed by DFT calculations. In this case a linear trimeric $(WO_3)_3$ cluster shown on top of Fig. 21 was employed as a model. Thermodynamically, the linear $(WO_3)_3$ isomer is slightly higher in energy as compared to the cyclic $(WO_3)_3$ trimer.[46, 69] Fig. 21 compares DFT calculations for dehydration of a single adsorbed ethanol molecule at each site. The terminal dioxo sites (blue, Fig. 21A) are identical in coordination environment with those in the cyclic trimer and as such exhibit similar Lewis acidities (fluoride affinities).[46] The net result is that the dissociative adsorption of ethanol into an ethoxy and a hydroxyl is found to be strongly exothermic and energetically similar to the same process on the cyclic trimer. Likewise, dehydration via the concerted C_α-O and C_β-H bond breaking exhibits similar energy barriers of about 30 kcal/mol.

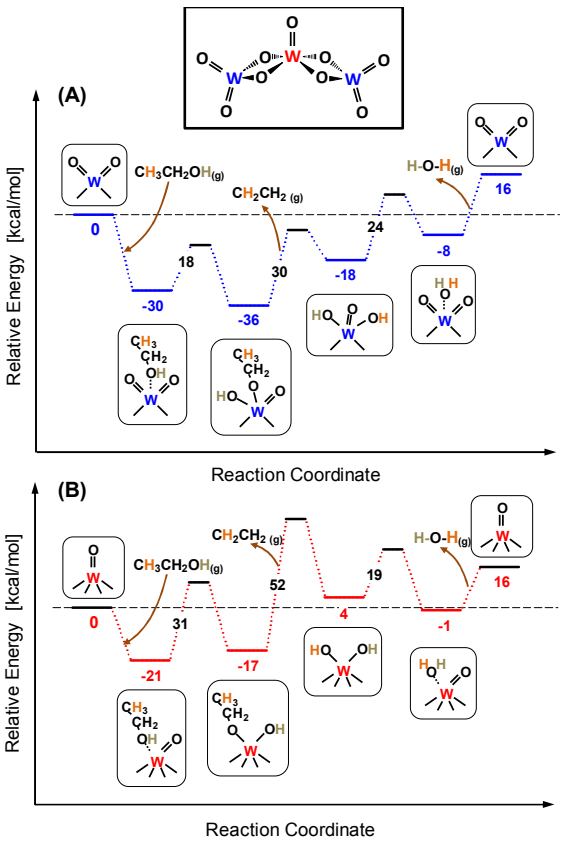

Fig. 21 Reaction mechanisms for the dehydration of a single ethanol molecule on the (a) dioxo O=W=O and (b) monooxo W=O moiety of the linear $(WO_3)_3$ cluster (shown on top) determined via DFT. Reprinted with permission from Li *et al.*[73]

Interestingly, the computed pathway for reactivity on the central monooxo species (red, Fig. 21B), which is coordinated by four O_b sites and one O_t site, is quite different. The computed fluoride affinity for this site is 20% lower than that for the dioxo sites.[46] This leads to weaker adsorption and an O-H dissociation step which is more than 10 kcal/mol higher in energy than desorption of the intact alcohol. Also, the C_α-O and C_β-H bond breaking step leading to the formation of ethylene is more than 20 kcal/mol higher in energy. Hence, the decreased Lewis acidity is expected to lead to a marked decrease in (and/or absence of) activity towards alcohol dehydration.

It is further noted, that the dehydration on the dioxo site is favored whether coordinated with one or two alcohol molecules.[73] However, analogous with the cyclic $(WO_3)_3$ clusters, adsorption of the second alcohol to form a weakly adsorbed water provides a kinetically facile pathway that facilitates the dehydration reaction. In contrast, on the monooxo site, the coordination with two alcohol molecules is not achievable due to steric reasons, further explaining the low activity of monooxo sites. In general, observations such as these support the conjecture that dioxo groups are required for catalytic dehydration of WO_3 based clusters whereas monooxo groups are chemically inactive.

6. Concluding Remarks

In summary, planar model and matrix isolated cluster studies of $(MO_3)_3$ based catalysts have provided a wealth of insight on the detailed structure, reactivity and energetics of these materials. In general, reactivity of these species towards organic molecules is found to be governed by the terminal M=O oxo groups with dioxo species shown to be necessary for catalytic reactions such as alcohol hydration and dehydrogenation. The stronger Lewis acidity of the W^{6+} sites relative to the Mo^{6+} analogue enhances the overall reactivity of these centers but the more easily reducible Mo^{6+} leads to a higher selectivity towards oxidation reactions (e.g. ethanol to acetaldehyde). Interestingly, the reaction yields on different substrates have been found to vary dramatically, primarily due the annihilation of dioxo groups as a result of differences in cluster binding. Surprisingly, no substrate induced changes have been observed in the overall energetics of observed reactions.

Despite the progress in terms of our comprehension of how these model catalysts operate, many important aspects of their activity are yet to be fully understood. For instance, there is a clear trend towards liberating protons during the course of reactions with alcohols which would imply that under steady state conditions these newly created Brønsted acidic sites may also have reactivity as has been proposed for polyoxometalate clusters.[40, 41] Whether the resulting protons are bound to bridge or terminal oxygen and how their relative acid strength is related to the reducibility of the metal sites remains an open question. This strongly motivates future reactivity studies done under steady state conditions (as opposed to TPD), which may help illuminate these issues. Additionally, studies at higher pressures that allow for higher steady state coverages of alcohols at elevated temperatures may shed further light on whether the monooxo species remain inactive.

There is also a strong indication based on TPD that the various reaction channels in these systems are strongly coupled, in that probe molecules such as ethanol undergo both dehydration, dehydrogenation and desorption (after proton scrambling) in concert. Comparative redox chemistry of supported W and Mo systems is yet to be fully explored to the level of detail as Lewis acidic induced processes. Further comparative experimental and theoretical work on structurally well characterized $(MO_3)_3$ clusters on oxide substrates that allow for a varied degree of charge transfer to the supported $(MO_3)_3$ should be of great value. In this respect, thin MgO(001) films with varied thickness and/or reducible oxides such as TiO_2, ZrO_2 RuO_2 and CeO_2 with different work functions represent great candidates for exploring such issues.

Acknowledgements

The authors would like to acknowledge many co-workers and collaborators that have been instrumental in producing a significant fraction of the results reviewed here, in particular A. Bondarchuk, Z. Fang, C. L. Guenther, M. S. Kelley, J. Kim, Y. K. Kim, S. Li, S. C. Li, Z. Li, V. Matolin, F. P. Netzer, B. Smid, R. S. Smith, J. M. White, and Z. Zhang. The work was supported by the U.S. Department of Energy Office of Basic Energy Sciences, Division of Chemical Sciences, Biosciences and Geosciences. PNNL is operated for the U.S. DOE by Battelle Memorial Institute under Contract No. DE-AC06-76RLO 1830. D. A. Dixon is indebted to the Robert Ramsay Endowment of The University of Alabama for partial support.

Notes and references

[a] Fundamental and Computational Sciences Directorate and Institute for Integrated Catalysis, Pacific Northwest National laboratory, PO Box 999, Richland, Washington 99352, USA

[b] Department of Chemistry, University of Alabama, Shelby Hall, Box 870336, Tuscaloosa, Alabama 35487, USA.

1. G. Deo and I. E. Wachs, *J. Phys. Chem.*, 1991, **95**, 5889-5895.
2. A. Corma, J. M. Lopeznieto, N. Paredes, M. Perez, Y. Shen, H. Cao and S. L. Suib, in *New Developments in Selective Oxidation by Heterogeneous Catalyses*, eds. P. Ruiz and B. Delmon, 1992, vol. 72, pp. 213-220.
3. Y. S. Yoon, N. Fujikawa, W. Ueda, Y. Morooka and K. W. Lee, *Catal. Today*, 1995, **24**, 327-333.
4. Y. S. Yoon, W. Ueda and Y. Morooka, *Top. Catal.*, 1996, **3**, 265-275.
5. S. Albonetti, F. Cavani and F. Trifiro, *Catal. Rev.-Sci. Eng.*, 1996, **38**, 413-438.
6. G. Busca, *Catal. Today*, 1996, **27**, 457-496.
7. F. C. Meunier, A. Yasmeen and J. R. H. Ross, *Catal. Today*, 1997, **37**, 33-42.
8. L. E. Cadus, M. F. Gomez and M. C. Abello, *Catal. Lett.*, 1997, **43**, 229-233.
9. J. Haber and E. Lalik, *Catal. Today*, 1997, **33**, 119-137.
10. W. L. Chu, T. Echizen, Y. Kamiya and T. Okuhara, *Appl. Catal. A-Gen.*, 2004, **259**, 199-205.
11. I. E. Wachs and K. Routray, *ACS Catal.*, 2012, **2**, 1235-1246.
12. M. Sun, J. Zhang, P. Putaj, V. Caps, F. Lefebvre, J. Pelletier and J.-M. Basset, *Chem. Rev.*, 2013, DOI: 10.1021/cr300302b.
13. D. G. Barton, M. Shtein, R. D. Wilson, S. L. Soled and E. Iglesia, *J. Phys. Chem. B*, 1999, **103**, 630-640.
14. R. D. Wilson, D. G. Barton, C. D. Baertsch and E. Iglesia, *J. Catal.*, 2000, **194**, 175-187.
15. V. Lebarbier, G. Clet and M. Houalla, *J. Phys. Chem. B*, 2006, **110**, 13905-13911.
16. V. Lebarbier, G. Clet and M. Houalla, *J. Phys. Chem. B*, 2006, **110**, 22608-22617.
17. W. Zhou, E. I. Ross-Medgaarden, W. V. Knowles, M. S. Wong, I. E. Wachs and C. J. Kiely, *Nature Chemistry*, 2009, **1**, 722-728.
18. W. Grunert, R. Feldhaus, K. Anders, E. S. Shpiro and K. M. Minachev, *J. Catal.*, 1989, **120**, 444-456.
19. S. L. Chen, Y. Wang, G. Yuan, D. Hua, M. Zheng and J. Zhang, *Chemical Engineering & Technology*, 2013, **36**, 795-800.
20. J. Macht, C. D. Baertsch, M. May-Lozano, S. L. Soled, Y. Wang and E. Iglesia, *J. Catal.*, 2004, **227**, 479-491.
21. R. L. Smith and G. S. Rohrer, *J. Catal.*, 1998, **173**, 219-228.
22. R. K. Grasselli, J. D. Burrington and J. F. Brazdil, *Faraday Discuss.*, 1981, **72**, 203-223.
23. R. K. Grasselli and J. D. Burrington, *Adv. Catal.*, 1981, **30**, 133-163.

24. P. Wehrer, S. Libs and L. Hilaire, *Appl. Catal. A-Gen.*, 2003, **238**, 69-84.
25. T. Matsuda, F. Uchijima, H. Sakagami and N. Takahashi, *Phys. Chem. Chem. Phys.*, 2001, **3**, 4430-4436.
26. J. Papp, S. Soled, K. Dwight and A. Wold, *Chem. Mater.*, 1994, **6**, 496-500.
27. J. P. Marcq, X. Wispenninckx, G. Poncelet, D. Keravis and J. J. Fripiat, *J. Catal.*, 1982, **73**, 309-328.
28. M. Li, E. I. Altman, A. Posadas and C. H. Ahn, *Thin Solid Films*, 2004, **446**, 238-247.
29. M. Li, W. Gao, A. Posadas, C. H. Ahn and E. I. Altman, *J. Phys. Chem. B*, 2004, **108**, 15259-15265.
30. I. E. Wachs, T. Kim and E. I. Ross, *Catal. Today*, 2006, **116**, 162-168.
31. D. J. Stacchiola, S. D. Senanayake, P. Liu and J. A. Rodriguez, *Chem. Rev.*, 2013, **113**, 4373-4390.
32. H. Kuhlenbeck, S. Shaikhutdinov and H. J. Freund, *Chem. Rev.*, 2013, **113**, 3986-4034.
33. O. Karslioglu, X. Song, H. Kuhlenbeck and H. Freund, *Top. Catal.*, 2013, **56**, 1389-1403.
34. B. M. Reddy, B. Chowdhury and P. G. Smirniotis, *Applied Catalysis A: General*, 2001, **211**, 19-30.
35. S. Eibl, B. C. Gates and H. Knozinger, *Langmuir*, 2001, **17**, 107-115.
36. P. Afanasiev, C. Geantet, M. Breysse, G. Coudurier and J. C. Vedrine, *J. Chem. Soc.-Faraday Trans.*, 1994, **90**, 193-202.
37. C. D. Baertsch, K. T. Komala, Y. H. Chua and E. Iglesia, *J. Catal.*, 2002, **205**, 44-57.
38. L. J. Burcham, L. E. Briand and I. E. Wachs, *Langmuir*, 2001, **17**, 6164-6174.
39. E. I. Ross-Medgaarden, I. E. Wachs, W. V. Knowles, A. Burrows, C. J. Kiely and M. S. Wong, *J. Am. Chem. Soc.*, 2009, **131**, 680-687.
40. M. J. Janik, J. Macht, E. Iglesia and M. Neurock, *J. Phys. Chem. C*, 2009, **113**, 1872-1885.
41. J. Macht, M. J. Janik, M. Neurock and E. Iglesia, *J. Am. Chem. Soc.*, 2008, **130**, 10369-10379.
42. E. L. Lee and I. E. Wachs, *J. Phys. Chem. C*, 2007, **111**, 14410-14425.
43. J. Berkowitz, W. A. Chupka and M. G. Inghram, *J. Chem. Phys.*, 1957, **27**, 85-86.
44. A. Azens, M. Kitenbergs and U. Kanders, *Vacuum*, 1995, **46**, 745-747.
45. S. Maleknia, J. Brodbelt and K. Pope, *J. Am. Soc. Mass Spectrom.*, 1991, **2**, 212-219.
46. S. G. Li and D. A. Dixon, *J. Phys. Chem. A*, 2006, **110**, 6231-6244.
47. X. Huang, H. J. Zhai, T. Waters, J. Li and L. S. Wang, *Angew. Chem., Int. Ed.*, 2006, **45**, 657-660.
48. X. Huang, H. J. Zhai, B. Kiran and L. S. Wang, *Angew. Chem., Int. Ed.*, 2005, **44**, 7251.
49. W. Weltner Jr and D. McLeod Jr, *J. Mol. Spectrosc.*, 1965, **17**, 276-299.
50. D. W. Green and K. M. Ervin, *J. Mol. Spectrosc.*, 1981, **89**, 145-158.
51. M. F. Zhou and L. Andrews, *J. Chem. Phys.*, 1999, **111**, 4230-4238.
52. W. D. Bare, P. F. Souter and L. Andrews, *J. Phys. Chem. A*, 1998, **102**, 8279-8286.
53. T. V. Iorns and F. E. Stafford, *J. Am. Chem. Soc.*, 1966, **88**, 4819-&.
54. D. L. Neikirk, J. C. Fagerli, M. L. Smith, D. Mosman and T. C. Devore, *J. Mol. Struct.*, 1991, **244**, 165-181.
55. W. D. Hewett, J. H. Newton and W. Weltner, *J. Phys. Chem.*, 1975, **79**, 2640-2649.
56. Q. Sun, B. K. Rao, P. Jena, D. Stolcic, Y. D. Kim, G. Gantefor and A. W. Castleman, *J. Chem. Phys.*, 2004, **121**, 9417-9422.
57. Z. Li, Z. Fang, M. S. Kelley, B. D. Kay, R. Rousseau, Z. Dohnalek and D. A. Dixon, *J. Phys. Chem. C.*, 2013, DOI: 10.1021/jp500255f.
58. Y. K. Kim, Z. Dohnálek, B. D. Kay and R. Rousseau, *J. Phys. Chem. C*, 2009, **113**, 9721-9730.
59. Z. Li, Z. Zhang, Y. K. Kim, R. S. Smith, F. Netzer, B. D. Kay, R. Rousseau and Z. Dohnalek, *J. Phys. Chem. C*, 2011, **115**, 5773-5783.
60. S. G. Li, J. M. Hennigan, D. A. Dixon and K. A. Peterson, *J. Phys. Chem. A*, 2009, **113**, 7861-7877.
61. K. A. Peterson, D. Feller and D. A. Dixon, *Theor. Chem. Acc.*, 2012, **131**, 1079.
62. D. Feller, K. A. Peterson and D. A. Dixon, *Mol. Phys.*, 2012, **110**, 2381-2399.
63. D. A. Dixon, D. Feller and K. A. Peterson, in *Annual Reports in Computational Chemistry*, ed. R. A. Wheeler, Elsevier, Amsterdam, 2012, vol. 8, pp. 1-28.
64. S. G. Li and D. A. Dixon, *J. Phys. Chem. A*, 2007, **111**, 11908-11921.
65. N. J. Mayhall, E. L. Becher, A. Chowdhury and K. Raghavachari, *J. Phys. Chem. A*, 2011, **115**, 2291-2296.
66. S. G. Li and D. A. Dixon, *J. Phys. Chem. C*, 2011, **115**, 19190-19196.
67. S. Li and D. A. Dixon, *J. Phys. Chem. A*, 2007, **111**, 11093-11099.
68. S. G. Li, H. J. Zhai, L. S. Wang and D. A. Dixon, *J. Phys. Chem. A*, 2009, **113**, 11273-11288.
69. S. G. Li, C. L. Guenther, M. S. Kelley and D. A. Dixon, *J. Phys. Chem. C*, 2011, **115**, 8072-8103.
70. S. Li and D. A. Dixon, in *New and Future Development in Catalysis: Catalysis by Nanoparticles*, ed. S. Suib, Elsevier, 2013, pp. 21-61.
71. Y. K. Kim, R. Rousseau, B. D. Kay, J. M. White and Z. Dohnálek, *J. Am. Chem. Soc.*, 2008, **130**, 5059-5061.
72. K. E. Gutowski and D. A. Dixon, *J. Phys. Chem. A*, 2006, **110**, 12044-12054.
73. Z. J. Li, B. Smid, Y. K. Kim, V. Matolin, B. D. Kay, R. Rousseau and Z. Dohnalek, *J. Phys. Chem. Lett.*, 2012, **3**, 2168-2172.
74. Y. K. Kim, B. D. Kay, J. M. White and Z. Dohnálek, *Catal. Lett.*, 2007, **119**, 1-4.
75. K. Kern, H. Niehus, A. Schatz, P. Zeppenfeld, J. George and G. Comsa, *Phys. Rev. Lett.*, 1991, **67**, 855-858.
76. P. Zeppenfeld, M. Krzyzowski, C. Romainczyk, G. Comsa and M. G. Lagally, *Phys. Rev. Lett.*, 1994, **72**, 2737-2740.
77. M. Wagner, S. Surnev, M. G. Ramsey, G. Barcaro, L. Sementa, F. R. Negreiros, A. Fortunelli, Z. Dohnalek and F. P. Netzer, *J. Phys. Chem. C*, 2011, **115**, 23480-23487.
78. U. Diebold, *Surf. Sci. Rep.*, 2003, **48**, 53-229.
79. C. L. Pang, R. Lindsay and G. Thornton, *Chem. Rev.*, 2013, **113**, 3887-3948.
80. Z. Dohnalek, I. Lyubinetsky and R. Rousseau, *Prog. Surf. Sci.*, 2010, **85**, 161-205.
81. O. Bondarchuk, X. Huang, J. Kim, B. D. Kay, L. S. Wang, J. M. White and Z. Dohnálek, *Angew. Chem., Int. Ed.*, 2006, **45**, 4786-4789.

82. J. Kim, O. Bondarchuk, B. D. Kay, J. M. White and Z. Dohnálek, *Catal. Today*, 2007, **120**, 186-195.
83. J. Zhu, H. Jin, W. J. Chen, Y. Li, Y. F. Zhang, L. X. Ning, X. Huang, K. N. Ding and W. K. Chen, *J. Phys. Chem. C*, 2009, **113**, 17509-17517.
84. J. Zhu, H. Jin, L. Zang, Y. Li, Y. Zhang, K. Ding, X. Huang, L. Ning and W. Chen, *J. Phys. Chem. C*, 2011, **115**, 15335-15344.
85. J. Zhu, H. Jin, Y. Li, X. Huang and Y. Zhang, *Acta Chimica Sinica*, 2011, **69**, 905-911.
86. C. Di Valentin, M. Rosa and G. Pacchioni, *J. Am. Chem. Soc.*, 2012, **134**, 14086-14098.
87. W. Weiss and W. Ranke, *Prog. Surf. Sci.*, 2002, **70**, 1-151.
88. N. Nilius, *Surf. Sci. Rep.*, 2009, **64**, 595-659.
89. S. K. Shaikhutdinov, R. Meyer, D. Lahav, M. Baumer, T. Kluner and H. J. Freund, *Phys. Rev. Lett.*, 2003, **91**, 076102.
90. Y. N. Sun, L. Giordano, J. Goniakowski, M. Lewandowski, Z. H. Qin, C. Noguera, S. Shaikhutdinov, G. Pacchioni and H. J. Freund, *Angew. Chem., Int. Ed.*, 2010, **49**, 4418-4421.
91. F. Ringleb, Y. Fujimori, H. F. Wang, H. Ariga, E. Carrasco, M. Sterrer, H. J. Freund, L. Giordano, G. Pacchioni and J. Goniakowski, *J. Phys. Chem. C*, 2011, **115**, 19328-19335.
92. Y. N. Sun, Z. H. Qin, M. Lewandowski, S. Kaya, S. Shaikhutdinov and H. J. Freund, *Catal. Lett.*, 2008, **126**, 31-35.
93. Q. Fu, W. X. Li, Y. X. Yao, H. Y. Liu, H. Y. Su, D. Ma, X. K. Gu, L. M. Chen, Z. Wang, H. Zhang, B. Wang and X. H. Bao, *Science*, 2010, **328**, 1141-1144.
94. Q. Fu, Y. X. Yao, X. G. Guo, M. M. Wei, Y. X. Ning, H. Y. Liu, F. Yang, Z. Liu and X. H. Bao, *Phys. Chem. Chem. Phys.*, 2013, **15**, 14708-14714.
95. Y. K. Kim, Z. R. Zhang, G. S. Parkinson, S. C. Li, B. D. Kay and Z. Dohnalek, *J. Phys. Chem. C*, 2009, **113**, 20020-20028.
96. S. C. Li, Z. Li, Z. Zhang, B. D. Kay, R. Rousseau and Z. Dohnalek, *J. Phys. Chem. C*, 2012, **116**, 908-916.
97. J. Goniakowski, C. Noguera, L. Giordano and G. Pacchioni, *Phys. Rev. B*, 2009, **80**, 125403.
98. L. Giordano and G. Pacchioni, *Acc. Chem. Res.*, 2011, **44**, 1244-1252.
99. J. Zhu, L. Giordano, S. Lin, Z. Fang, Y. Li, X. Huang, Y. Zhang and G. Pacchioni, *J. Phys. Chem. C*, 2012, **116**, 17668-17675.
100. H. J. Freund and G. Pacchioni, *Chem. Soc. Rev.*, 2008, **37**, 2224-2242.
101. T. Risse, S. Shaikhutdinov, N. Nilius, M. Sterrer and H. J. Freund, *Acc. Chem. Res.*, 2008, **41**, 949-956.
102. G. Pacchioni and H. Freund, *Chem. Rev.*, 2013, **113**, 4035-4072.
103. M. Sterrer, T. Risse, U. M. Pozzoni, L. Giordano, M. Heyde, H. P. Rust, G. Pacchioni and H. J. Freund, *Phys. Rev. Lett.*, 2007, **98**, 096107.
104. M. Sterrer, T. Risse, M. Heyde, H. P. Rust and H. J. Freund, *Phys. Rev. Lett.*, 2007, **98**, 206103.
105. V. Simic-Milosevic, M. Heyde, N. Nilius, T. Konig, H. P. Rust, M. Sterrer, T. Risse, H. J. Freund, L. Giordano and G. Pacchioni, *J. Am. Chem. Soc.*, 2008, **130**, 7814.
106. X. Lin, B. Yang, H. M. Benia, P. Myrach, M. Yulikov, A. Aumer, M. A. Brown, M. Sterrer, O. Bondarchuk, E. Kieseritzky, J. Rocker, T. Risse, H. J. Gao, N. Nilius and H. J. Freund, *J. Am. Chem. Soc.*, 2010, **132**, 7745-7749.
107. D. Ricci, A. Bongiorno, G. Pacchioni and U. Landman, *Phys. Rev. Lett.*, 2006, **97**, 036106.
108. A. Hellman, S. Klacar and H. Gronbeck, *J. Am. Chem. Soc.*, 2009, **131**, 16636.
109. A. Gonchar, T. Risse, H. J. Freund, L. Giordano, C. Di Valentin and G. Pacchioni, *Angew. Chem., Int. Ed.*, 2011, **50**, 2635-2638.
110. H. Gronbeck, *J. Phys. Chem. B*, 2006, **110**, 11977-11981.
111. J. Zhu, S. J. Lin, X. W. Wen, Z. X. Fang, Y. Li, Y. F. Zhang, X. Huang, L. X. Ning, K. N. Ding and W. K. Chen, *J. Chem. Phys.*, 2013, **138**.
112. L. Abelmann and C. Lodder, *Thin Solid Films*, 1997, **305**, 1-21.
113. A. L. Barabasi and H. E. Stanley, *Fractal Concepts in Surface Growth*, Cambridge University Press, Cambridge, 1995.
114. G. A. Kimmel, K. P. Stevenson, Z. Dohnálek, R. S. Smith and B. D. Kay, *J. Chem. Phys.*, 2001, **114**, 5284-5294.
115. G. A. Kimmel, Z. Dohnálek, K. P. Stevenson, R. S. Smith and B. D. Kay, *J. Chem. Phys.*, 2001, **114**, 5295-5303.
116. Z. Dohnálek, G. A. Kimmel, P. Ayotte, R. S. Smith and B. D. Kay, *J. Chem. Phys.*, 2003, **118**, 364-372.
117. D. W. Flaherty, Z. Dohnálek, A. Dohnalkova, B. W. Arey, D. E. McCready, N. Ponnusamy, C. B. Mullins and B. D. Kay, *J. Phys. Chem. C*, 2007, **111**, 4765-4773.
118. Z. Dohnálek, G. A. Kimmel, D. E. McCready, J. S. Young, A. Dohnalkova, R. S. Smith and B. D. Kay, *J. Phys. Chem. B*, 2002, **106**, 3526-3529.
119. D. W. Flaherty, N. T. Hahn, R. A. May, S. P. Berglund, Y. M. Lin, K. J. Stevenson, Z. Dohnalek, B. D. Kay and C. B. Mullins, *Acc. Chem. Res.*, 2012, **45**, 434-443.
120. K. P. Stevenson, G. A. Kimmel, Z. Dohnálek, R. S. Smith and B. D. Kay, *Science*, 1999, **283**, 1505-1507.
121. J. Kim, Z. Dohnálek and B. D. Kay, *Surf. Sci.*, 2005, **586**, 137-145.
122. H. van Kranenburg and C. J. Lodder, *Mater. Sci. Eng. R*, 1994, **11**, 295.
123. K. Robbie and M. J. Brett, *J. Vac. Sci. Technol. A*, 1997, **15**, 1460-1465.
124. K. Robbie, M. J. Brett and A. Lakhtakia, *Nature*, 1996, **384**, 616.
125. K. Robbie, C. Shafai and M. J. Brett, *J. Mater. Res.*, 1999, **14**, 3158-3163.
126. B. Smid, Z. Li, A. Dohnalkova, B. W. Arey, R. S. Smith, V. Matolin, B. D. Kay and Z. Dohnalek, *J. Phys. Chem. C*, 2012, **116**, 10649-10655.
127. Z. X. Lu, S. M. Kanan and C. P. Tripp, *J. Mater. Chem.*, 2002, **12**, 983-989.
128. O. Bondarchuk, Y. K. Kim, J. M. White, J. Kim, B. D. Kay and Z. Dohnálek, *J. Phys. Chem. C*, 2007, **111**, 11059-11067.
129. Y. K. Kim, B. D. Kay, J. M. White and Z. Dohnálek, *Surf. Sci.*, 2008, **602**, 511-516.

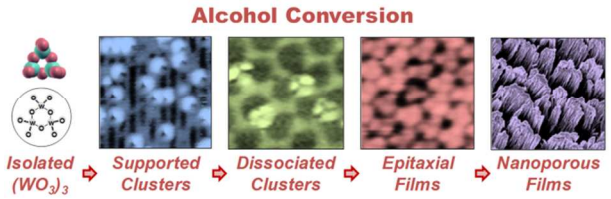

The review summarizes recent synthesis and reactivity studies of model oxide catalysts prepared by employing gas phase cyclic $(WO_3)_3$ and $(MoO_3)_3$ clusters.

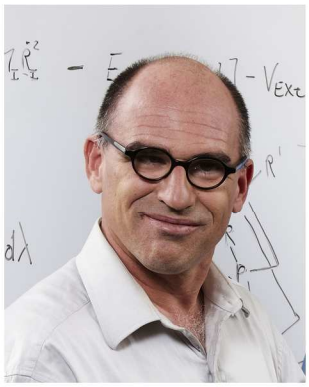

Roger Rousseau

Dr. Roger Roussau obtained his Ph.D. in Chemistry from the University of Michigan in 1995 in theoretical solid state inorganic chemistry followed by postdoctoral studies at MPI-Stuttgart in the group of Prof. Michele Parrinello from 1996-1998. Currently he is a senior scientist in the Institute for Integrated Catalysis at Pacific Northwest National Laboratory where his reaserch efforts focus on thoery and computational as pertains to modeling catalytic processes. His interest lie in employingg ab initio molecular dyanmics, microkinetics and stastical mechanics methods for modeling chemical reactivity for heterogeneaus catalysis.

Bruce Kay

Dr. Bruce D. Kay is a Laboratory Fellow in the Chemical Physics and Analysis group at Pacific Northwest National Laboratory and a member of the Institute for Integrated Catalysis. He received a B.S. in Chemistry from the University of Illinois (1976) and a Ph.D. in Chemical Physics from the University of Colorado (1982). From 1982 to 1991, he was on the technical staff at Sandia National Laboratory prior to joining PNNL in November 1991. His research focuses on the application of molecular beam scattering and surface analysis techniques to problems in interfacial and condensed phase chemical kinetics and dynamics.

David Dixon

Dr. David A. Dixon is the Robert Ramsay Chair at the Department of Chemistry, University of Alabama (UA), where he has been since 2004. Prior to moving to UA, he was at the Pacific Northwest National Laboratory, DuPont Central Research, and the University of Minnesota. His main research interest is the development and application of computational chemistry to solve chemical problems in the areas of catalysis, geochemistry, biochemistry of peptides, heavy element chemistry for technology applications, chemical hydrogen storage materials, and fluorine and main group chemistry.

Zdenek Dohnalek

Dr. Zdenek Dohnálek is a Senior Scientist in the Institute for Integrated Catalysis at Pacific Northwest National Laboratory (PNNL). He received his Ph.D. in physical chemistry at the University of Pittsburgh in 1997 and was a postdoctoral fellow at PNNL from 1998 to 2000. His research focuses on experimental studies of fundamental model systems that are necessary to understand chemical transformations in heterogeneous catalysis and environment. His studies employ novel deposition methods for the preparation of model systems that can be probed using both high-resolution imaging and ensemble-averaged spectroscopies and allow for a detailed, molecular level understanding of system structure and reactivity.